Bioactive Materials 48 (2025) 55–70

Contents lists available at ScienceDirect

Bioactive Materials

journal homepage: www.keaipublishing.com/en/journals/bioactive-materials

cGAMP-targeting injectable hydrogel system promotes periodontal restoration by alleviating cGAS-STING pathway activation

Xiang Liu [a,b,c,1], Hua Zhang [d,1], Lei Xu [a,b,1], Huayu Ye [a,b], Jinghuan Huang [e], Jing Xiang [a,b], Yunying He [a,b], Huan Zhou [f], Lingli Fang [a,b], Yunyan Zhang [a,b], Xuerong Xiang [a,b,*], Richard D. Cannon [g], Ping Ji [a,b,**], Qiming Zhai [a,b,***]

[a] College of Stomatology, Chongqing Medical University, Chongqing, China
[b] Chongqing Key Laboratory of Oral Diseases, Chongqing, China
[c] Department of Stomatology, The Second Affiliated Hospital, Chongqing Medical University, Chongqing, China
[d] Department of Obstetrics and Gynaecology, The First Affiliated Hospital of Chongqing Medical University, Chongqing, China
[e] Orthopedic Department of Shanghai Sixth People's Hospital, Shanghai, China
[f] Key Laboratory of Shaanxi Province for Craniofacial Precision Medicine Research, College of Stomatology, Xi'an Jiaotong University, Xi'an, China
[g] Department of Oral Sciences, Sir John Walsh Research Institute, Dentistry, University of Otago, Dunedin, 9054, New Zealand

ARTICLE INFO

Keywords:
cGAMP homeostasis
cGAS-STING pathway
Inflammatory environment
Periodontal ligament stem cells
Osteogenic differentiation
Injectable hydrogel system

ABSTRACT

The impaired function of periodontal ligament stem cells (PDLSCs) impedes restoration of periodontal tissues. The cGAS-cGAMP-STING pathway is an innate immune pathway that sensing cytosolic double-stranded DNA (dsDNA), but its role in regulating the function of PDLSCs is still unclear. In this study, we found that mitochondrial DNA (mtDNA) was released into the cytoplasm through the mitochondrial permeability transition pore (mPTP) in PDLSCs upon inflammation, which binds to cGAS and activated the STING pathway by promoting the production of cGAMP, and ultimately impaired the osteogenic differentiation of PDLSCs. Additionally, it is first found that inflammation can down-regulate the level of the ATP-binding cassette membrane subfamily member C1 (ABCC1, a cGAMP exocellular transporter) and ectonucleotide pyrophosphatase/phosphodiesterase 1 (ENPP1, a cGAMP hydrolase), which further aggravated the accumulation of intracellular cGAMP, leading to the persistent activation of the cGAS-STING pathway and thus the impaired the differentiation capacity of PDLSCs. Furthermore, we designed a hydrogel system loaded with a mPTP blocker, an ABCC1 agonist and ENPP1 to promote periodontal tissue regeneration by modulating the production, exocytosis, and clearance of cGAMP. In conclusion, our results highlight the profound effects, and specific mechanisms, of the cGAS-STING pathway on the function of stem cells and propose a new strategy to promote periodontal tissue restoration based on the reestablishment of cGAMP homeostasis.

1. Introduction

Periodontitis, a chronic inflammatory disorder, is mainly initiated by the dysbiosis of oral microbial ecology [1,2]. Oral microorganisms activate host and microbiota interactions, leading to an overactive and persistent proinflammatory immune response, resulting in destruction of the periodontium, and eventually tooth loss [3]. Periodontal ligament stem cells (PDLSCs), as mesenchymal stem cells (MSCs) located in periodontal ligaments [4], are crucial for maintaining periodontal homeostasis and promoting periodontal tissue regeneration and recovery [5]. However, the inflammatory environment compromises the osteogenic differentiation ability of PDLSCs, thus impeding the restoration of periodontal tissues even after removal of the inflammatory stimuli [6]. Therefore, there is an urgent need to elucidate the cellular and

Peer review under the responsibility of KeAi Communications Co., Ltd.
* Corresponding author. Stomatological Hospital of Chongqing Medical University, Chongqing Key Laboratory of Oral Diseases, Chongqing, 401174, China.
** Corresponding author. Stomatological Hospital of Chongqing Medical University, Chongqing Key Laboratory of Oral Diseases, Chongqing, 401174, China.
*** Corresponding author. Stomatological Hospital of Chongqing Medical University, Chongqing Key Laboratory of Oral Diseases, Chongqing, 401174, China.
E-mail addresses: 500067@hospital.cqmu.edu.cn (X. Xiang), jiping@hospital.cqmu.edu.cn (P. Ji), zhaiqm@hospital.cqmu.edu.cn (Q. Zhai).
[1] These authors contributed equally to this work and should be considered co-first authors.

https://doi.org/10.1016/j.bioactmat.2025.02.010
Received 28 September 2024; Received in revised form 29 January 2025; Accepted 6 February 2025
Available online 13 February 2025

molecular mechanisms responsible for the impaired osteogenic differentiation ability of PDLSCs in order to facilitate periodontal tissue repair.

The cyclic GMP-AMP synthase (cGAS)-stimulator of interferon genes (STING) signaling pathway is crucial for triggering innate immune response and defending pathogens via sensing double-strain DNA [7,8]. Moreover, recently various studies evidenced that cGAS-STING pathway also participate in many non-infectious diseases, even independent of activating inflammation [9]. Those studies suggested that cGAS-STING pathway holds novel exciting functions beyond immune regulation. It has been reported that mtDNA released from damaged mitochondria activates cGAS-STING pathway and leads to cellular injury [10,11]. Our previous study also identified that impaired mitochondrial function and mitophagy are responsible for the compromised osteogenic differentiation ability of MSCs upon inflammatory stimuli [12]. However, whether and how the cGAS-STING pathway participates in regulating the function of PDLSCs remains to be discovered.

When mtDNA released from mitochondria and sensed by cGAS, cGAS stimulate the synthesis of the secondary messenger cyclic GMP-AMP (cGAMP), which then activates the STING and mediates the downstream pro-inflammatory responses [13]. Notably, under physiological conditions, cGAMP can be eliminated by several mechanisms to avoid exaggerated inflammatory response. For example, some specific channels, such as those in the LRRC8 protein family [14,15] and ATP-binding cassette transporter ABCC1 [16], could extracellularly transport cGAMP. And ectonucleotide pyrophosphatase/phosphodiesterase 1 (ENPP1) mediates the degradation of cGAMP [17]. Therefore, the process from cGAMP production to cGAMP exportation and degradation play a critical role in the regulation of the cGAS-STING signaling, suggesting that targeting cGAMP homeostasis could be a novel therapeutic strategy for diseases associated with cGAS-STING pathway activation, especially in the restoration of PDLSCs function and periodontal tissue in periodontitis.

In this study, we clarified the activation of cGAS-STING pathway impeded the osteogenic differentiation ability of PDLSCs. Mechanistically, we evidenced that inflammation not only resulted in the mtDNA released from mitochondria into cytoplasm through mitochondrial permeability transition pore (mPTP) channels, but also inhibited the exportation and degradation of cGAMP. Both mechanisms contributed to the over-activation of the cGAS-STING pathway and impaired the osteogenic differentiation of PDLSCs. Therefore, we fabricated a linear polyethylene glycol poly (azelaic acid glycerol ester) (PEGA) hydrogel system loaded with cyclosporin A (CsA, a mPTP blocker), ABCC1 agonist thiethylperazine (TT) and ENPP1(CsA-TT-ENPP1@PEGA) that could be injected locally into periodontal tissue. This triple-functional hydrogel system effectively reduced the level of cGAMP in PDLSCs upon inflammation and showed significant promise as an effective therapy for periodontal bone defects, with potential implications for the management of other diseases via intervention of cGAMP homeostasis (Fig. 1).

2. Materials and methods

2.1. Reagents

All reagents were obtained commercially. α-MEM medium, Fetal Bovine Serum (FBS), trypsin, streptomycin and penicillin were obtained from Gibco (USA); Cell Counting Kit-8(CCK8, cat #C0037), Alkaline phosphatase test kit (cat #P0321S), Mitochondrial separation reagent (cat #C3601), BCA Protein Assay Kit (cat #P0010), Mitochondrial transition pore assay kit (cat #C2009S) and Genomic DNA Purification Mini Spin Kit (cat #D0063) were obtained from Beyotime (China); LPS (cat #L2630), Cetylpyridinium chloride (CPC, cat #C0732), RU360 (cat

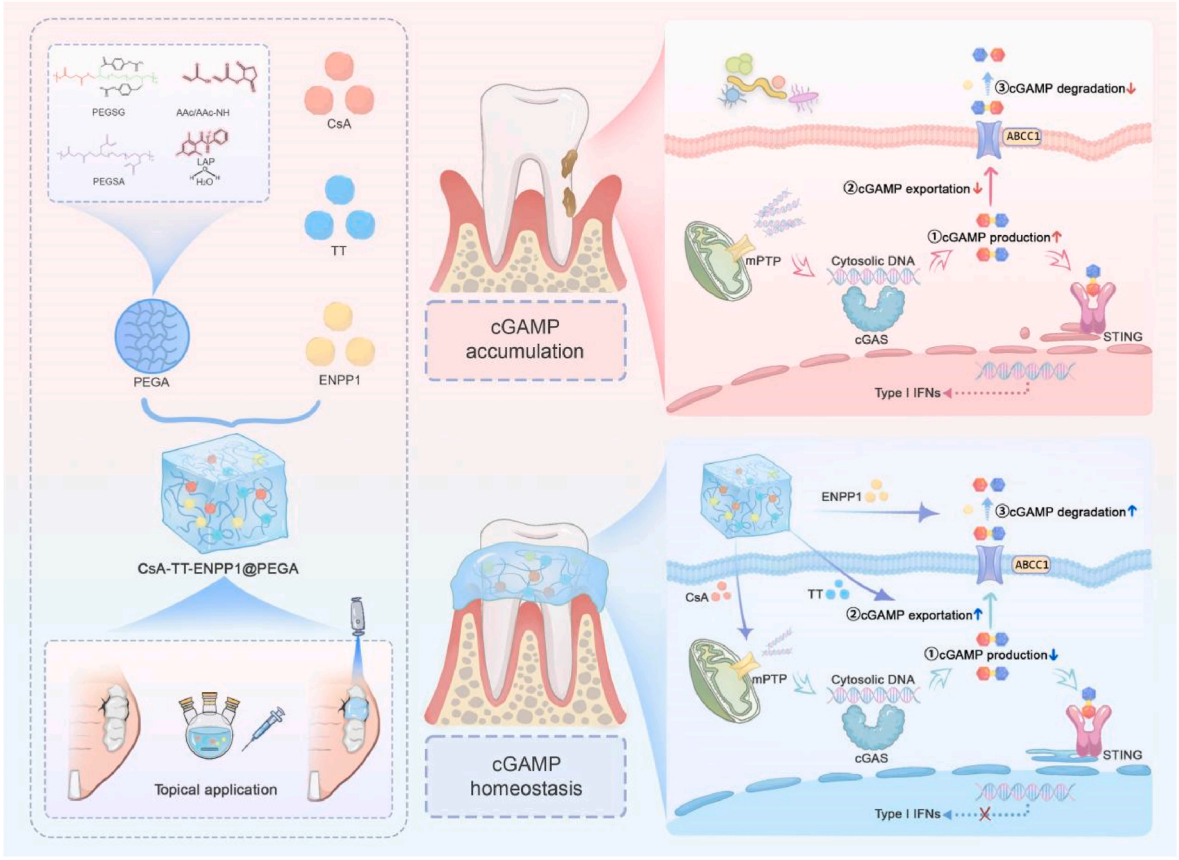

Fig. 1. Schematic representation of how CsA-ABCC1-ENPP1@PEGA hydrogel restore the cGAMP homeostasis, and thus block cGAS-STING pathway to rescue the function of PDLSCs to facilitate periodontal recovery.

#557440) and Alizarin-Red S (cat #A5533) were obtained from Sigma (USA); C-176 (cat #HY-112906), EtBr (cat #HY-D0021), CsA (cat #HY-B0579), 8-OHdG (cat #HY-P81140), sodium pyruvate (cat #HY-W015913) and uridine (cat #HY-B1449) were obtained from Med Chem Express (MCE, China); Collagenase Type I (cat #C8140), β-glycerophosphate (cat #IG1340), ascorbic acid (cat #A8100), and dexamethasone (cat #D8040) were purchased from Solarbio (China); cGAMP ELISA kits (FANKEW, China, cat #F11293-A); IL-6 (Cat#0049A), TNF-α (Cat#0122A) and IFN-α (Cat#0464A) ELISA kits were purchased from Jiangsu Meibiao Biotechnology Co.,Ltd; The primary antibody anti-dsDNA mouse monoclonal was purchased from PROGEN (Germany, cat#AC-30-10). Lipo3000™ Liposomal Transfection Reagent (cat #L3000008), MitoSOX detection kits (cat #M36009) and TMRM assay kit (cat #I34361) were purchased from Thermo Scientific (USA); RNA isolation kit (Takara Biology, Japan), TB green PCR Master Mix (Takara, Japan); Rhod-2 AM (cat #40776 ES, Yeasen, China). Primary antibodies: cGAS (Cell Signaling Technology (CST), USA; cat #79978S), STING (CST; cat #13647S), TBK1 (Abcam, USA; cat #ab40676), IRF3 (Abcam, USA; cat #ab68481), p-IRF3 (Abcam, USA; cat #ab320082), VDAC (PTM BIO, China; cat #PTM-6935), HK2 (PTM BIO, China; cat #PTM-5371), BAX (PTM BIO, China; cat #PTM-5482), CD34 (Biolegend, USA, cat #378602), CD90 (Biolegend, USA, cat #109502), CD44 (Biolegend, USA, cat #109502), CD31 (Biolegend, USA, cat #109502), Anti-dsDNA antibody (PROGEN, China, cat #AC-30-10), Alexa Fluor® 488 secondary antibody (cat #ab150077) and Alexa Fluor® 594 secondary antibody (cat #150080) were purchased from Abcam (USA); The HRP-conjugated secondary antibody was purchased from ZSGB BIO (China, cat #ZB-2306).

2.2. Cell culture

Consent forms were obtained before conducting this research project. Healthy tooth samples were collected from 6 individuals, aged 18–30 years. Donor information is listed in Table S1 in the Supporting Information. PDLSCs were isolated as previously described [18]. Briefly, periodontal ligament tissue was scraped from the middle third of the root surface, and then digested with collagenase I (3 mg/mL) at 37 °C for 60 min. Then the tissue fragments were cultured in α-MEM with 10 % FBS, 100 mg/mL of streptomycin, and 100 units/mL of penicillin at 37 °C in 5 % CO_2. The culture medium was refreshed every 3 days. To verify the cells' mesenchymal origin, PDLSCs at the third passage were digested with trypsin and resuspended in PBS at a concentration of 2×10^6 cells/mL. The cells were incubated with CD34, CD90, CD44 and CD31 in the dark at 37 °C for 60 min, according to the manufacturer's instructions. Then the cells were washed twice with PBS and analyzed with a flow cytometer (BD Biosciences, USA). PDLSCs from passage 3 to passage 5 were used in this study (H-PDLSCs). Based on our previous work [19] and established protocols from other studies [20,21], LPS was administered at a concentration of 10 μg/mL for 7 days to simulate the inflammatory micro-environment in PDLSCs.

2.3. Osteogenic differentiation assay

Cells were cultured in 24-well microtiter plates and induced to differentiate with mineralization induction medium, which was composed of α-MEM medium, 10 % FBS, β-glycerophosphate (10 mM), ascorbic acid (50 μM), and dexamethasone (0.1 μM). The medium was changed every 3 days. After 7 days induction, alkaline phosphatase (ALP) staining was performed. Alizarin red (AR) staining and semi-quantitative analysis were performed after 21 days.

Before ALP and ARS staining, the cell samples were washed with PBS and fixed with 4 % paraformaldehyde for 20 min. Then, the fixed cells were stained with AR for 5 min at room temperature (RT) or stained with ALP solution for 30 min at RT. For the quantification of mineralized nodules, 300 μL 10 % CPC were added into each well for 15min at RT and the absorbance at 570 nm was measured with a microplate reader (EnSpire, PerkinElmer, Singapore).

2.4. CCK8 assay

To verify the cytotoxicity of TT, 5000 PDLSCs were seeded in the wells of 96-well plates and incubated at 37 °C, 5 % CO_2 overnight. Then, the culture medium was replaced with 100 μL α-MEM containing TT at different concentrations (100, 50, 20, 10, 5, 1, or 0.5 μg/mL). After 24h incubation, cells were washed with PBS and incubated with 100 μL fresh α-MEM and 10 μL CCK8 solution at 37 °C for another 2-h. Finally, the absorbance at 450 nm was measured using a microplate reader (EnSpire, PerkinElmer).

2.5. Enzyme-linked immunosorbent assay (ELISA)

To assess the concentrations of intracellular and extracellular cGAMP, as well as the secretion of pro-inflammatory cytokines, such as IL-6, TNF-α and IFN–α in each group of cells, the supernatant at day 1, 3, 5 and 7 were collected and assayed using ELISA kits according to the manufacturer's instructions. The absorbance at 450 nm was measured. The concentrations of cGAMP, IL-6, TNF-α and IFN-α were calculated based on a standard curve and normalized to the cell protein concentration.

2.6. RNA interference

siRNA specifically targeting STING (siSTING) was obtained from ObiO (China). Lipo3000™ Liposomal Transfection Reagent was used to transfect the PDLSCs with the siSTING, according to the manufacturer's instructions, and a nonspecific siRNA provided by the same supplier was used as a negative control. After transfection, qRT-PCR was conducted to verify the transfection efficiency, and the transfected cells were stimulated according to the experimental requirements. The specific siRNA sequences used in this study are listed in Table S2.

2.7. Cytosolic DNA detection and quantification

To detect cytosolic DNA, cells stimulated with LPS (10 μg/mL for 7 days), or not, were seeded in confocal dishes overnight, and then incubated with Mito-Tracker for 30 min at 37 °C. Subsequently, cells were fixed with 4 % paraformaldehyde for 10 min, washed with PBS, and maintained in blocking buffer (PBS containing 10 % goat serum and 0.3 % Triton X) for 30 min. Cell samples were then stained with anti-dsDNA antibody (PROGEN, Germany, cat#AC-30-10) at 4 °C overnight and stained with Alexa Fluor 488 goat anti-mouse IgG secondary antibody (1:400) for 1 h at RT. Nuclei were visualized with a 15-min 4 0,6-diamidino-2-phenylindole (DAPI) stain. Images of cells were acquired with a confocal microscope (Leica, Germany). The analyses of images were performed using Image J (National Institutes of Health, USA).

To further verify the source of cytosolic DNA, we first extracted the cytosolic DNA as previously reported [22]. In brief, mitochondrial separation reagent was used to remove mitochondria from PDLSCs, and then a Universal Genomic DNA Purification Mini Spin Kit was used to extract nucleic acid from the cells without mitochondria. We then quantified the cytoplasmic mtDNA by qRT-PCR as previously reported [23], a Dounce homogenizer was used to homogenize 1×10^7 cells which were then centrifuged at 800 g for 5 min at 4 °C. The volume of the supernatant was normalized according to the protein concentration, and the mixture was then centrifuged at 10,000 g for 30 min at 4 °C to generate a supernatant corresponding to the cytosolic fraction, and DNA was isolated from 200 μL of the cytosolic fraction. qRT-PCR was conducted on both the D-loop to measure mtDNA content and β2m to measure genomic DNA content. The amount of D-loop and β2m DNA in cytosolic extracts was normalized to Glyceraldehyde-3-phosphate dehydrogenase (GAPDH) and calculated by the change-in-threshold method [$2^{\wedge(-\Delta\Delta CT)}$]. The sequences of the primers used are listed in

Table S3.

2.8. Quantitative real-time PCR (qRT-PCR)

Total RNA was obtained with a total RNA isolation kit and used for reverse transcription. qRT-PCR was then performed using TB green PCR Master Mix. The target gene expression was normalized to the GAPDH level and calculated by the change-in-threshold method [$2^{\wedge(-\Delta\Delta CT)}$]. The sequences of the primers used in the experiment are listed in Table S4.

2.9. Western blot (WB) analysis

Cells were lysed in a RIPA lysis buffer containing a protease inhibitor cocktail (Beyotime, China), and the protein concentration in the lysates was measured with a BCA Protein Assay Kit. Equivalent amounts of proteins sample were loaded onto 10 % SDS-PAGE gels for electrophoresis, and then electroblotted onto 0.45 mm PVDF membranes (Millipore, USA) at 220 mA. Membranes were blocked with 5 % skim milk for 2 h at RT, and then incubated with primary antibodies overnight at 4 °C. Next, the membranes were incubated with HRP-conjugated secondary antibodies for 1 h at RT. Finally, the immunoreactive bands were visualized by an Immobilon Western HRP Substrate (Millipore, USA). Image J (NIH, USA) was used for the grayscale analysis of western blots.

2.10. Mitochondrial function assay

The mitochondrial membrane potential (MMP) was measured with a TMRM assay kit. Briefly, PDLSCs were incubated with 100 nM TMRM for 30 min at 37 °C. For mitochondrial ROS detection, cells were loaded with 4 mM MitoSOX for 30 min according to the manufacturer's instructions. Following staining, cells were resuspended in PBS and analyzed with a flow cytometer (BD Biosciences, USA). Representative live-cell images were captured using an EVOS microscope.

The oxygen consumption rate (OCR) and extracellular acidification rate (ECAR) was measured using an XF24 Extracellular Flux Analyzer (Agilent Technologies, USA). Briefly, cells were loaded onto XF24 cell culture microplates and subjected to the Mito Stress Test or Glycolysis Stress Test using the protocol provided (Agilent Technologies, USA). For the Mito Stress Test, basal respiration was measured, then the mitochondria were treated sequentially with 10 mM adenosine diphosphate (Sigma), 2 μM oligomycin (Agilent Technologies), 5 μM carbonyl cyanide-p-trifluoromethoxy phenyl-hydrazone (Agilent Technologies), and then a mixture of rotenone and antimycin A (0.5 μM; Agilent Technologies). As for the Glycolysis Stress Test, the basal glycolysis was measured, then the mitochondria were treated sequentially with 10 mM glucose (Agilent Technologies), 1 μM oligomycin (Agilent Technologies), 10 mM 2-deoxidation glucose (Agilent Technologies).

2.11. Mitochondrial permeability transition pore assay

To analyze mPTP opening, cells treated as indicated (10 μg/ml LPS with 50 μM RU360 or not) were assessed using a mitochondrial transition pore assay kit. Briefly, cells were stained with 1 mM calcein acetoxymethyl ester (calcein-AM), 1 mM Hoechst, and 4 mM $CoCl_2$ for 30 min at 37 °C. After washing twice with PBS, fluorescence intensity was determined using a flow cytometer (BD Biosciences, USA), and the images were acquired with a Zeiss confocal microscope.

2.12. Detection of mitochondrial Ca^{2+} levels

The mitochondrial Ca^{2+} concentration was measured by the fluorescence intensity of the mitochondrial calcium-specific fluorescent probe Rhod-2 AM. Briefly, cells were stained with Rhod-2 AM (4 μM) for 30 min at 37 °C. Following the incubation, the cells were washed with PBS for three times and then incubated for an additional 30 min at 37 °C. Then, the Ca^{2+} fluorescence intensity was detected by flow cytometry and representative images were acquired with a Zeiss confocal microscope.

2.13. Transmission electron microscopy (TEM)

To collect cells for TEM, PDLSCs were centrifuge for 10 min at 10000 g, and then fixed with 2 % glutaraldehyde. Following the fixation, the cells were dehydrated in a graded ethanol series, embedded in situ in epoxy resin and cut into 10 μM sections, afterwards, ultrathin sections were stained with uranyl acetate for 30 min and lead citrate for 10 min, and observed by an FEI Tecnai G12 Spirit BioTwin transmission electron microscope (FEI Company, USA).

2.14. Mitochondrial DNA-depleted cells

Depletion of mtDNA was performed using a relevant culture medium containing 100 ng/mL EtBr, 100 μg/mL sodium pyruvate and 50 μg/mL uridine as previously described [23]. PDLSCs were cultured in this medium for one day. The depletion was analyzed using real-time qRT-PCR to measure the expression of mitochondrial genes or nuclear genes. The primer sequences used are provided in Table S3.

2.15. Immunofluorescence (IF) staining

Cell was fixed in 4 % paraformaldehyde for 15min, and then permeabilized with 0.1 % Triton X-100 for another 15 min. Subsequently, samples were incubated with anti-STING or 8-OHdG antibodies overnight at 4 °C, followed by incubation with the corresponding secondary antibody and DAPI. The IF images were captured using a Zeiss confocal microscope. 3D surface plots were analyzed with Image J (NIH, USA). Higher peaks indicated more robust infiltration.

2.16. RNA sequencing

Cells from the group of H-PDLSCs and H-PDLSCs + LPS were collected with Trizol for transcriptome analysis. RNA extraction, purification, reverse transcription, library construction, and sequencing were all performed by NovelBio Corp. Laboratory (Shanghai, China). Differentially expressed genes (DEGs) were screened out by "limma" package based on the comparison of expression profiles between H-PDLSCs samples and H-PDLSCs + LPS samples. The screening criteria for DEGs were as follows: log2 fold-change (FC) should be greater than 1 or less than −1 and p-value <0.05. Heatmaps based on differentially expressed genes were drawn by the software TB tools (Version 2.096). Functional enrichment analysis of DEGs and gene set enrichment analysis (GSEA) was performed by the R package "clusterProfiler" (Version 4.12.0).

2.17. Preparation of double bonded polyether dilated poly (azelaic acid) fatty triol esters

Azelaic acid and tetrabutylammonium hydroxide were added to 95 % ethanol at a molar ratio of 1:2, and the reaction was stirred at 40–70 °C (preferably 50–55 °C) for 20–40min (preferably 25–35 min), and the ethanol and water were removed at the end of the reaction to obtain product 1. Subsequently, under the protection of a nitrogen atmosphere, azelaic acid, polyether diol diglycidyl ether and product 1 with the molar ratio of 1:1:0.006 were dissolved in anhydrous N, N-dimethylformamide, and the reaction was stirred at 80–150 °C (preferably 90–120 °C) for 48–96h (preferably 60–84h), to obtain the product 2. Dialysis of the product 2 was carried out to obtain the desired precursor polymer: Polyether dilated poly (azelaic acid) fatty triol ester.

Double bonded polyether dilated poly (azelaic acid) fatty triol esters were obtained by replacing the side hydroxyl group on the precursor polymer with a double bond-containing modifying substance. Specifically, under the protection of a nitrogen atmosphere, the precursor

polymer and triethylamine were dissolved in anhydrous N, N-dimethylformamide at a molar ratio of 1:1∼1:2, and then 0.5–2 eq acryloyl chloride was slowly added dropwise, and the reaction stirred at 0 °C for 12 h. At the end of the reaction, the extract was filtered, and settle with ether, and then dialysis and purification, to obtain the said double-bonded polyether-dilated poly (nonane dioic acid) fatty triol ester.

2.18. Preparation and characterization of PEGA hydrogel

To construct the hydrogel, solutions of PEGA and lithium phenyl-2,4,6-trimethylbenzoylphosphinate (LAP; 0.07 %, 0.7 % or 7 % w/v in deionized water) were mixed with deionized water at a volume ratio of 3:7 and ultrasonic cracking for 5 min to form a photocurable aqueous solution. For the fabrication of drug-loaded PEGA hydrogel, 12 μg CsA, 1 μg TT and 0.1 μg ENPP1 were mixed with 30 μL PEGA hydrogel and ultrasonic cracking for another 5 min. To characterize the hydrogel, PEGA hydrogel with different LAP concentrations were imaged via SEM. In brief, the samples were placed on the holders, and after gold sputter coating (about 45s at 10 mA), the samples were imaged via SEM (Sigma 300, ZEISS, Germany) at 3 kV. EDS element mapping and spectra of the samples were generated with an SEM equipped with EDS at 15 kV. FTIR spectra (4000-400 cm^{-1}) were collected on a FTIR spectroscope (Nicolet iS20, Nicolet, USA), Raman analysis was performed with a confocal Raman microscope (CRM) (Alpha300R, WITec GmbH, Germany) equipped with a TEM single-frequency laser (λ = 532 nm, laser power = 40 mW, WITec GmbH). FTIR and Raman data were recorded as absorbance units. Rheological tests were carried out using a rotational rheometer (Haake Mars40, German) at 25 °C. The stiffness of different PEGA hydrogels was investigated by testing the storage (G′) and loss (G′′) moduli over a range of 10–0.1 rad/s and 5 % strain amplitude over time by a frequency sweep, as well as over a range of 6 rad/s and 5 % strain amplitude by a time sweep. Moreover, the injectable property of the hydrogel was demonstrated both *in vivo* and *in vitro* by filling with different sizes and shapes.

2.19. Degradation analysis

For the swelling and degradation tests of PEGA hydrogel, 30 mg PEG powder were gelled with LAP solution under blue light irradiation and weighted (W1). Then, the hydrogel was soaked in 1 ml PBS and weighed at a predetermined time point (W2). The swelling and degradation ratio was calculated as described previously [24]:

$$\text{Swelling and Degradation ratio (\%)} = (W2 - W1)/W1 \times 100\% \quad (1)$$

For the volumetric swelling tests of PEGA hydrogel, PEGA suspension was injected into a container and irradiated with blue light, then its length (L), width (W) and height (H) were measured and calculated as the original volume (V1). Afterwards, the hydrogel was soaked in 1 ml PBS and measured at a predetermined time point (V2). The volumetric swelling ratio was calculated as follows:

$$\text{Volumetric swelling ratio (\%)} = (V2 - V1)/V1 \times 100\% \quad (2)$$

2.20. Characterization of drug release from hydrogels

The release kinetics of the PEGA hydrogels were evaluated using doxycycline (DOX). In brief, 10 μL DOX (2 mg/mL) was mixed with 200 mg PEG to form a DOX-loaded PEGA hydrogel. Then, the drug-loaded hydrogel was placed in PBS (500 μL, pH 7.4). At the predetermined time points, 100 μL supernatant was collected and the same volume of PBS added to maintain a constant volume. The absorbance at 480 nm was measured to calculate the concentration of DOX, and the cumulative release of DOX was calculated according to the following equation:

$$\text{Cumulative release ratio (\%)} = (M_n + \text{Mn-1} + \ldots\ldots + M_1) * V/M \times 100\% \quad (3)$$

where M represents the total mass of the drug in the PEGA hydrogel, M_n represents the concentration of released drug during sampling at time n, and V represents the replacement volume of PBS.

2.21. Experimental periodontitis model

C57BL/6 mice were purchased from the Animal Research center of Chongqing Medical University and housed under specific pathogen-free (SPF) conditions at the animal experimental center of the Stomatological Hospital of Chongqing Medical University. As reported previously [25], experimental periodontitis was induced in mice by placing a ligature around the maxillary second molar for one week. The mice were checked every day in case of loosening or displacement. One week later, only those mice with obvious gingival swelling and alveolar bone resorption were included in the subsequent study.

Mice with periodontitis were randomly divided into the following four groups and treated according to their group (n = 5): (1) Control group (no treatment), (2) Lig + Saline group (ligature-induced experimental periodontitis and saline injection), (3) Lig + CsA group (ligature-induced experimental periodontitis and CsA injection (10 mg/kg)) [26,27] and (4) Lig + C176 group (ligature-induced experimental periodontitis and C176 injections, 750 nmol per mouse in 200 μL corn oil) [28,29]. According to the group, 30 μl drug or PBS were injected at 6 sites (5 μL per site) around the maxillary second molar: in the mesiobuccal gingiva, distobuccal gingiva, mesiopalatal gingiva, distopalatal gingiva, mesial and distal gingival papilla [30]. All the above treatments were repeated daily, and the mice were euthanized to harvest the maxillary jaws of periodontitis mice for histological analysis after 7 days treatment.

Mice with periodontitis were also randomly divided into the following groups: Control group (no treatment), PEGA group (periodontitis with simple hydrogel injection) and CsA-ABCC1-ENPP1@PEGA group (periodontitis with CsA-ABCC1-ENPP1-loaded hydrogel injection). The mixture of CsA, TT, ENPP1 and PEGA was injected around the maxillary second molar and received blue light radiation (about 5 s) to form the CsA-ABCC1-ENPP1@PEGA hydorgel. After one week of healing, the mice were euthanized, and periodontal tissue harvested to assess healing.

In another experiment, 8-week-old $STING^{-/-}$ and WT C57BL/6 male mice were divided into four groups (n = 5): (1) $STING^{+/+}$ control group (WT with no treatment), (2) $STING^{-/-}$ control group ($STING^{-/-}$ mice with no treatment), (3) $STING^{+/+}$ ligature group (WT with ligature-induced experimental periodontitis), (4) $STING^{-/-}$ ligature group ($STING^{-/-}$ mice with ligature-induced experimental periodontitis). Experimental periodontitis was induced in mice with a ligature for 1 week and then they were allowed to recover for 1 week. After this, all the mice were euthanized to harvest the maxillary jaws for histological analysis.

2.22. Micro CT analysis and quantitative bone resorption analysis

Mice were euthanized by CO_2 hypoxia post-operation. The maxillae were harvested and fixed in 4 % paraformaldehyde for 24 h, then scanned by micro-CT (vivaCT80, SCANCO Medical AG, Switzerland) and a 3D reconstruction was performed simultaneously. The region of interest was a cuboidal alveolar bone encompassing the second molar, with a length extending from the most distal aspect of the upper first molar (M1) root to the most mesial aspect and upper second molar (M3) root. The width extended from the most buccal to the most palatal aspect of the M2 roots, and the height extended from the ABC to the M2 root apical. The CEJ-ABC distance, BV/TV %, Tb.Th and Tb.N were quantified with the SCANCO VivaCT40 micro-CT software.

2.23. Histological analysis

After Micro-CT analysis, the mandible bone samples were decalcified in 17 % ethylenediaminetetraacetic acid (EDTA, pH 8.0) for 1 month and then dehydrated by immersion in increasing concentrations of ethanol (60–100 %). Subsequently, the specimens were embedded in paraffin and cut into 6-μm sections. Sections were de-paraffinized following standard procedures, and then hematoxylin and eosin (H&E) staining was performed to detect the alveolar bone loss. For immunostaining, tissue sections were incubated with primary antibodies at 4 °C overnight and incubated with the corresponding secondary antibody for 1 h at RT on the next day, nuclei were stained with DAPI. All images were acquired with a Zeiss confocal microscope, and relative quantitative analyses were performed with Image-J.

2.24. In vivo compatibility

To test the long-term safety of CsA, CsA and CsA-ABCC1-ENPP1@PEGA were injected into the gingival for one month respectively. Afterwards, the heart, liver, spleen, lung and kidney of mice in the control group and the experimental group (injection of CsA or CsA-ABCC1-ENPP1@PEGA) were collected and dehydrated by immersion in increasing concentrations of ethanol (60–100 %). Subsequently, the specimens were embedded in paraffin and cut into 6-μm sections. Sections were de-paraffinized following standard procedures and then performed H&E staining to detect whether there were any abnormalities in the major organs following the application of CsA.

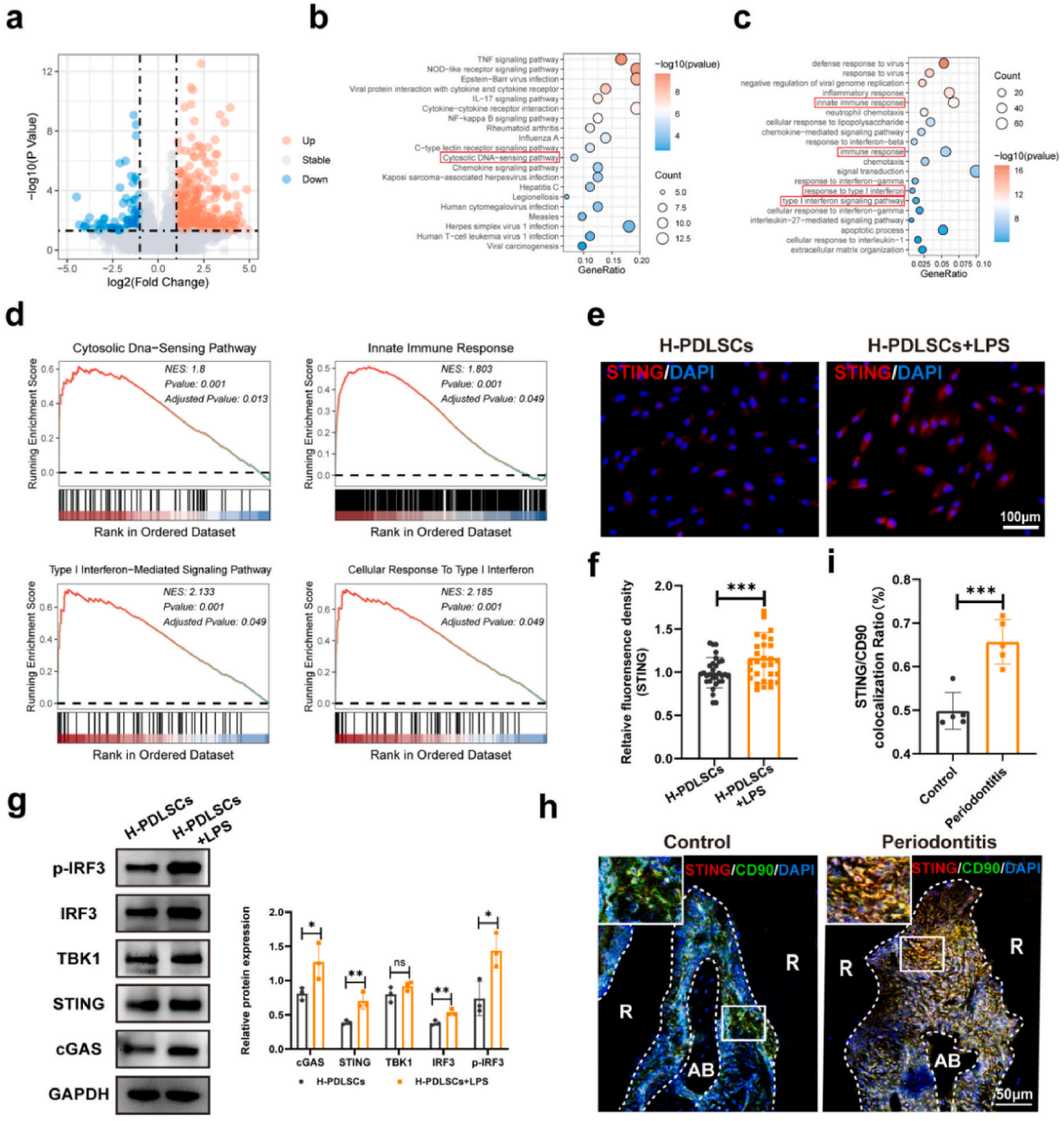

Fig. 2. The cGAS-STING pathway was activated in PDLSCs under inflammatory conditions. (a) Volcano plot of gene expression in H-PDLSCs and H-PDLSCs + LPS. **(b)** The KEGG pathway enrichment analysis **(c)** GO enrichment and **(d)** GSEA analysis after LPS treatment. **(e)** IF and quantitative analysis (f) of STING in H-PDLSCs and H-PDLSCs + LPS. Scale bar, 100 μm. n = 30 cells in each group (10 cells quantified per replicate). **(g)** WB analysis of proteins involved in the cGAS-STING pathway. **(h)** IF staining of PDLSCs (CD90, green) and STING (red) in periodontal tissueand. R: root, AB: alveolar bone. Scale bar, 50 μm. **(i)** Quantified the expression of STING in (h).

2.25. Statistical analysis

All experiments were repeated independently at least three times, and the data were plotted as mean ± standard deviation (SD). Data was analyzed using IBM SPSS Statistics 22. The student's *t*-test (two tailed) and one-way analysis of variance (ANOVA) were used to determine the statistical significance. Differences were considered statistically significant at $^{*}P < 0.05$, very significant for $^{**}P < 0.01$, and the most significant for $^{***}P < 0.001$.

3. Results

3.1. The cGAS-STING pathway was activated in PDLSCs under inflammatory conditions

In this study, PDLSCs were isolated from healthy periodontal ligaments (H-PDLSCs) (Fig. S1), and treated with lipopolysaccharide (LPS) for 7 days to simulate a chronic inflammatory micro-environment (H-PDLSCs + LPS). First, the transcriptomic analysis was performed to elucidate the mechanisms underlying periodontitis. The volcano plot showed that many genes were upregulated under inflammatory conditions (Fig. 2a). The Kyoto Encyclopedia of Genes and Genomes (KEGG) pathway enrichment analysis (Fig. 2b), gene ontology (GO) enrichment (Fig. 2c) and GSEA (Gene Set Enrichment Analysis) analysis (Fig. 2d) of the differentially expressed genes (DEGs) indicated that exposure to LPS elevated the cytosolic DNA-sensing pathway, type 1 interferon signaling pathway and interferon related innate immune response, which were associated with cGAS-STING signaling pathway. Subsequently, we investigated whether the cGAS-STING pathway was activated in inflammatory PDLSCs. IF staining confirmed that LPS stimulation promoted the expression of STING (Fig. 2e and f). WB analysis also showed that the protein expression of the cGAS-STING axis was increased in the H-PDLSCs + LPS group (Fig. 2g). The sub-cellular localization of STING is closely related to its activation status [31], and we observed an increase of perinuclear translocation of STING after stimulated by LPS (Fig. S2a). Moreover, the secretion of pro-inflammatory cytokines, such as IL-6, TNF-α, IFN-α, was significantly increased in H-PDLSCs + LPS (Fig. S2b). The expression of the STING in CD90 marked PDLSCs was also elevated in mice with ligature-induced periodontitis (Fig. 2h and i). Together, these results indicated the activation of the cGAS-STING pathway in inflammation-induced PDLSCs.

3.2. Inhibiting cGAS-STING pathway improved PDLSCs osteogenic differentiation and periodontal restoration

To confirm the role of the cGAS-STING pathway in PDLSC dysfunction, PDLSCs were transfected with small interfering RNA (siRNA) to knockdown STING expression (Fig. S3a). As expected, knockdown of STING significantly improved the differentiation ability of PDLSCs under inflammatory conditions (Fig. 3a, Fig. S3b). Moreover, we also applied STING knockout ($STING^{-/-}$) mice to detect the effect of STING inhibition in periodontal restoration (Fig. 3b). IF staining showed that STING deletion significantly reduced the expression of IRF3 in CD90 marked PDLSCs in the mice with ligature-induced periodontitis (Fig. 3c, Fig. S4a). Micro-computed tomography (micro-CT) was then conducted to quantify alveolar bone loss after 14 days (ligature-induced periodontitis for 7 days and removal of ligature for another 7 days). We found that ligature-induced alveolar bone resorption was significantly attenuated in $STING^{-/-}$ mice (Fig. 3d), with a decreased CEJ-ABC distance, increased BV/TV and increased trabecular numbers (Tb.N) (Fig. 3e). Moreover, H151, a highly potent and selective small molecule antagonist of STING, was used to evaluate the impact of STING inhibition on the osteogenic differentiation of PDLSCs *in vitro*. We found that H151 significantly reduced the expression of STING and downstream pathway proteins (Fig. 3f), and significantly alleviated the osteogenic differentiation deficiency of PDLSCs under inflammatory conditions (Fig. 3g, Fig. S4b). To further explore the effect of pharmacological inhibitor of STING in periodontal restoration, C176 was injected into six sites around the second molars of the mice after a week of periodontitis induction (Fig. 3h). We found that C176 significantly attenuated alveolar bone loss in mice with periodontitis (Fig. 3i and j). Taken together, the *in vitro* and *in vivo* experiments confirmed that the activation of the cGAS-STING pathway is closely associated with periodontitis, and suppression of STING has great potential for the treatment of periodontitis.

3.3. mtDNA released from damaged mitochondria is responsible for the activation of cGAS-STING pathway in PDLSCs upon inflammation

Mitochondria are known to play a central role in cell differentiation [32] and the progression of periodontitis [33]. Previous studies have reported that mtDNA released from damaged mitochondria can activate the cGAS-STING pathway [34]. Therefore, to investigate the mitochondrial function, Seahorse Bioscience XF Analyzer was applied to examine the oxygen consumption (OCR) and extracellular acidification rate (ECAR) as indicators of metabolic activity. The results showed that LPS strongly impaired the oxygen consumption of PDLSCs (Fig. 4a) while enhancing glycolytic activity (Fig. S5), indicating a shift in mitochondrial metabolism from oxidative phosphorylation to glycolysis under inflammatory conditions. Confocal microscopy images showed disturbed mitochondrial network in H-PDLSCs + LPS with more and prolonged mitochondria than in H-PDLSCs (Fig. 4b and c). Moreover, mitochondrial reactive oxygen species (mtROS) are a vital indicator of mitochondrial function, and we observed a significantly higher cellular mtROS level in the H-PDLSCs + LPS group (Fig. 4d, Fig. S6a and b). Consistent with the cellular mtROS level, the expression of antioxidant genes in the H-PDLSCs + LPS group was also significantly lower than that in the H-PDLSCs group (Fig. S7a), accompanied by decreased MMP in PDLSCs upon inflammation (Fig. 4e, Fig. S6c and d).

Double-stranded DNA (dsDNA), including damaged mtDNA, released into the cytoplasm, are critical factors that activate the cGAS-STING pathway. 8-Hydroxy-2′-deoxyguanosine (8-OHdG), an indicator for DNA oxidative damage, was highly expressed in the H-PDLSCs + LPS group (Fig. 4f). Consistently, the expression of the DNA oxidative damage repair enzyme 8-Oxoguanine DNA glycosylase 1 (OGG1) was significantly lower in PDLSCs after LPS stimulation (Fig. S7b). Moreover, the co-localization of dsDNA and mitochondria decreased in the H-PDLSCs + LPS group (Fig. 4g and h), qRT-PCR further suggested that there was more mtDNA released into the cytoplasm upon inflammation (Fig. 4i).

To further clarify whether the activation of cGAS-STING pathway and the PDLSC dysfunction was associated with mtDNA leakage, we depleted the mtDNA of PDLSCs with ethidium bromide (EtBr), a compound that is used to block the replication of mtDNA rather than nuclear DNA [35]. We found that EtBr treatment significantly reduced mtDNA copy number (Fig. S8a), and inhibited the activation of the cGAS-STING pathway in the H-PDLSCs + LPS group (Fig. 4j). More importantly, EtBr treatment partially alleviated the osteogenic differentiation deficiency of PDLSCs in the inflammatory micro-environment (Fig. 4k, Fig. S8b). These results indicated that inflammatory stimulation induced mtDNA damage and release into the cytoplasm, which further activated the cGAS-STING pathway and resulted in PDLSCs dysfunction.

3.4. mtDNA released into the cytosol via the mPTP channel in PDLSCs upon inflammation

It has been reported that apoptosis can induce the Bak/Bax permeabilization of the outer mitochondrial membrane and result in mtDNA leakage [36]. However, we did not observe a significant increase in apoptosis or in expression of BAX in LPS-treated cells in this study (Fig. 5a and b). On the contrary, the expression of mPTP related proteins HK2 and VDAC were significantly increased (Fig. 5b), suggesting that inflammation stimulation may alter the mPTP status. It is well known

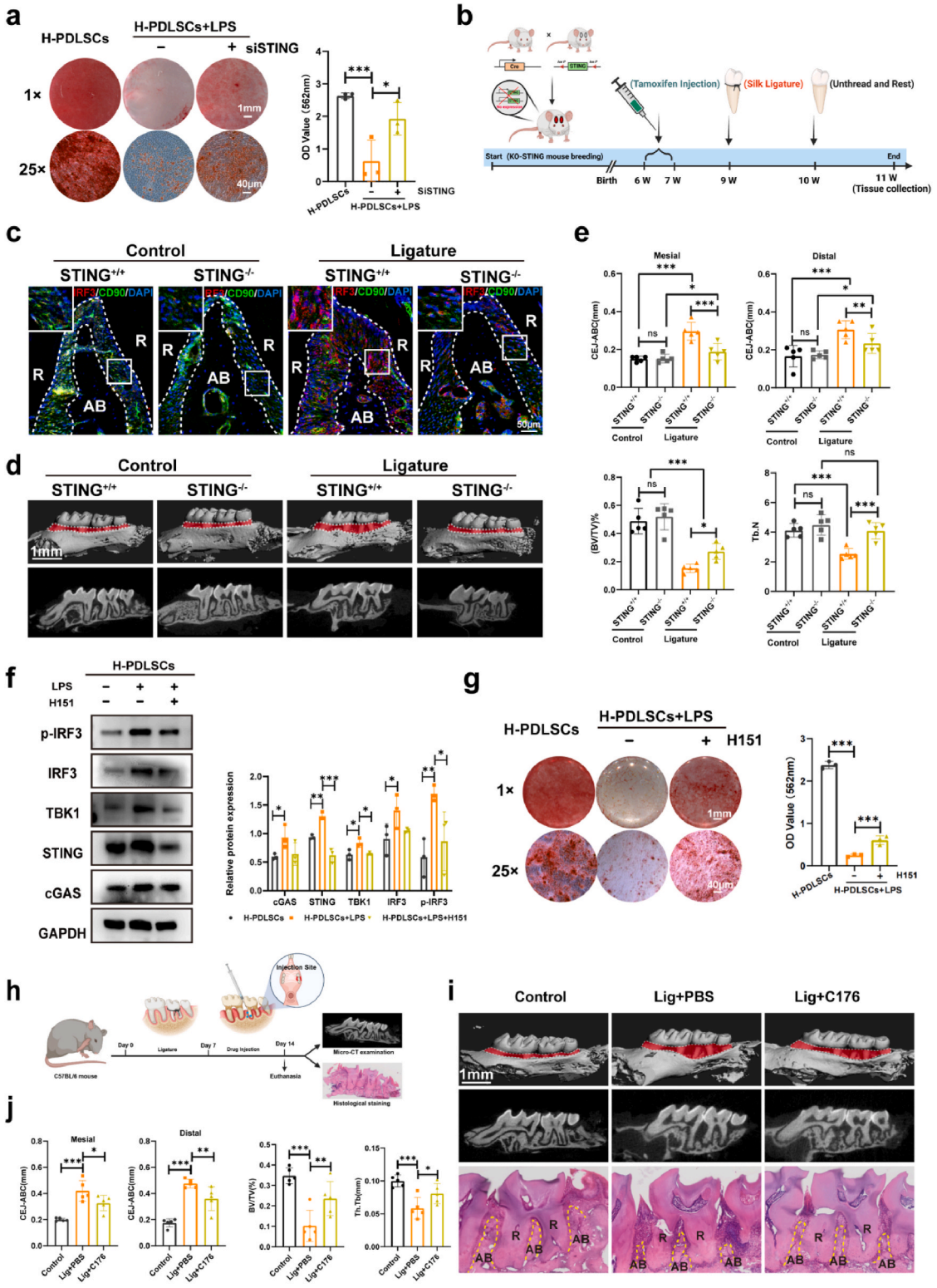

Fig. 3. Inhibiting cGAS-STING pathway improved PDLSC osteogenic differentiation and periodontal restoration. (a) siRNA-mediated STING knockdown improved the osteogenic differentiation of H-PDLSCs + LPS cells. **(b)** Schematic diagram of the treatment of STING$^{-/-}$ mice. **(c)** IF staining of PDLSCs (CD90, green) and IRF3 (red) in the periodontal tissue of mice from the different treatment groups. R: root, AB: alveolar bone. Scale bar, 50 μm. **(d)** Representative Macro-CT images of the alveolar bone of mice. **(e)** Quantitative analysis of the CEJ-ABC, BV/TV % and Th.N. **(f)** WB analysis of proteins involved in the cGAS-STING pathway after H151 treatment. **(g)** Alizarin Red staining and quantitative analysis of mineralized nodules after H151 treatment. **(h)** Schematic diagram of C176 treatment of ligature-induced periodontitis in C57 mice. **(i)** Representative images of Macro-CT and H&E is staining of the alveolar bone of mice from different treatment groups. The red color indicates root exposure. R: root, AB: alveolar bone. Scale bar, 1 mm. **(j)** Quantitative analysis of the CEJ-ABC, BV/TV % and Th.Tb. $^{*}P < 0.05$, $^{**}P < 0.01$, $^{***}P < 0.001$, ns, not significant.

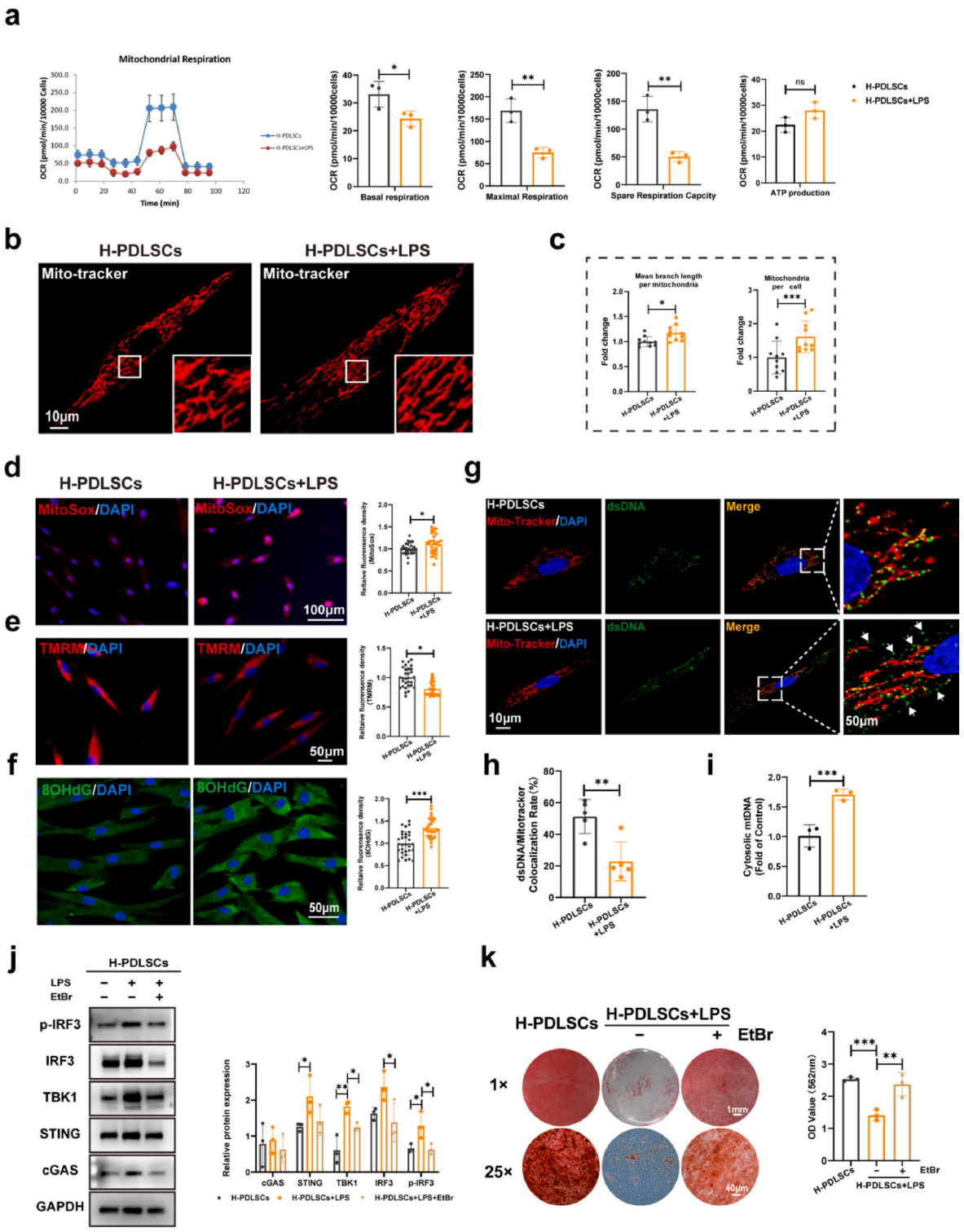

Fig. 4. cGAS-STING pathway activation was associated with cytoplasmic release of mitochondrial DNA. **(a)** Mitochondrial respiratory capacity analysis (oxygen consumption rate; OCR) measured with a Seahorse XFe24 analyzer. **(b)** Representative images of mitochondria stained with Mito Tracker. Scale bar, 10 μm. **(c)** Mitochondrial morphology (branch length and number per cell) analysis (n = 10 cells in each group). **(d)** IF and quantitative analysis of MitoSox staining. Scale bar, 100 μm. n = 30 cells in each group (10 cells quantified per replicate). **(e)** IF and quantitative analysis of ▲Ψm (TMRM staining). Scale bar, 50 μm. n = 30 cells in each group (10 cells quantified per replicate). **(f)** IF and quantitative analysis of 8-OHdG staining. Scale bar, 50 μm. n = 30 cells in each group (10 cells quantified per replicate). **(g)** IF staining of mitochondria (Mito Tracker, red) and DNA (anti-dsDNA antibody, green). White boxed regions in the panels are enlarged. The white arrows indicate dsDNA outside mitochondria. Scale bar, 10 μm. **(h)** Co-localization analysis of data from (g). **(i)** qRT-PCR analysis to detect the source of cytosolic DNA. **(j)** WB analysis of proteins in the cGAS-STING pathway after mtDNA depletion. **(k)** Alizarin Red staining and quantitative analysis of mineralized nodules. $^{*}P < 0.05$, $^{**}P < 0.01$, $^{***}P < 0.001$, ns, not significant.

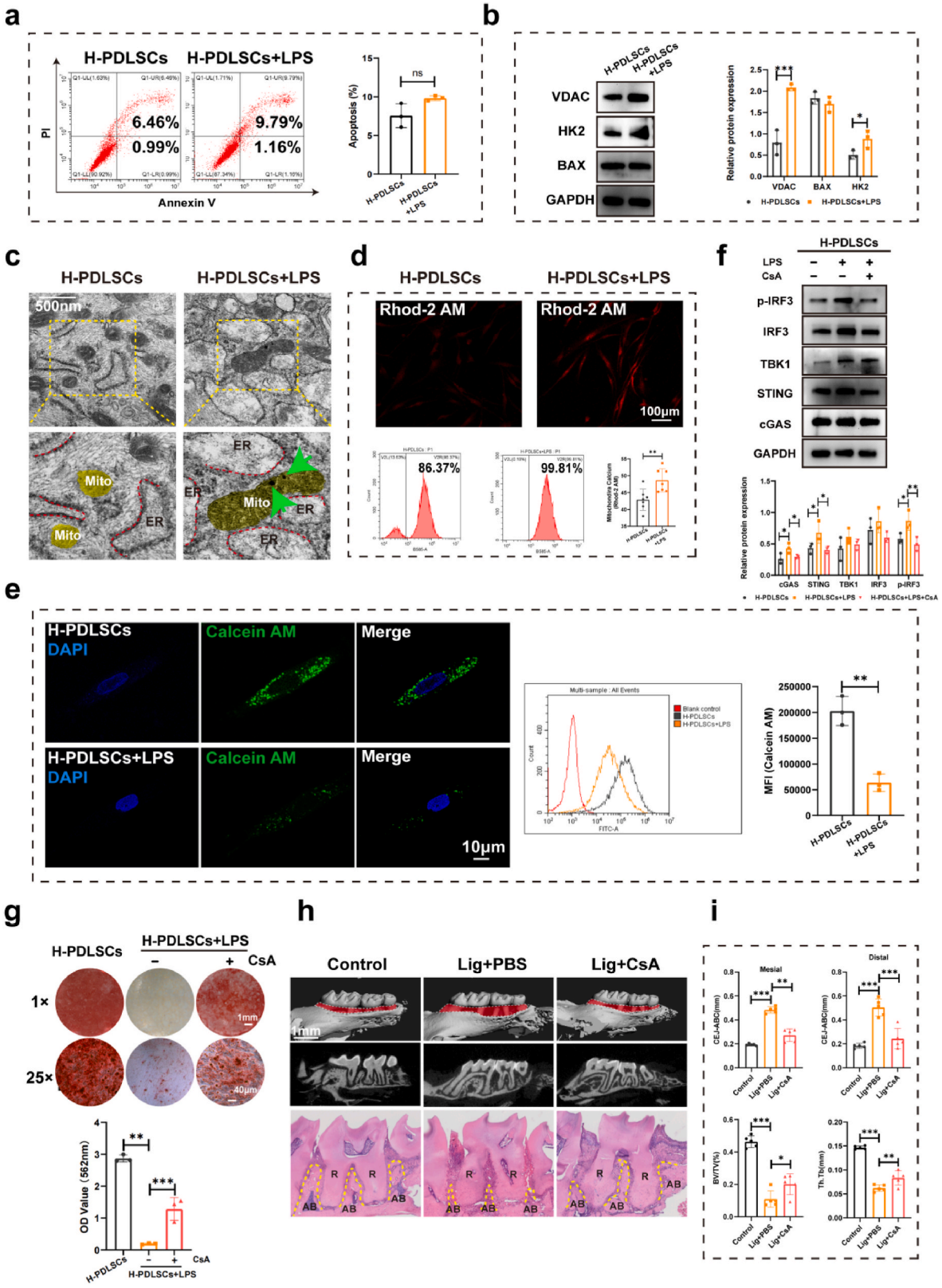

Fig. 5. Inflammatory stimulation triggers mtDNA release into the cytoplasm via the mPTP channel. **(a)** Apoptosis was detected by PI staining and flow cytometry. **(b)** WB analysis of BAX, VDAC, and HK2 expression. **(c)** Representative TEMs of H-PDLSCs and H-PDLSCs + LPS. Structures colored yellow indicate mitochondria, Structures delineated with red dashed line are endoplasmic reticulum, green arrows indicate matrix particle. Scale bar, 500 nm. **(d)** The mitochondrial Ca^{2+} was determined by Rhod-2 AM staining and quantitative analysis by flow cytometry. Scale bar, 10 μm. **(e)** The mPTP opening was determined by Calcein AM and quantitative analysis of MFI by flow cytometry. Scale bar, 10 μm. **(f)** WB analysis of proteins in the cGAS-STING pathway after CsA treatment. **(g)** Alizarin Red staining and quantitative analysis of mineralized nodules. **(h)** Representative Macro-CT images and H&E is staining of the alveolar bone of mice from different treatment groups. R: root, AB: alveolar bone. **(i)** Quantitative analysis of the CEJ-ABC, BV/TV % and Th.Tb. $^{*}P < 0.05$, $^{**}P < 0.01$, $^{***}P < 0.001$, ns, not significant.

that mitochondrial Ca^{2+} signaling profoundly influences mitochondrial homeostasis, such as mitochondrial oxidative phosphorylation, and ROS production [37]. In addition, mitochondrial Ca^{2+} overloading can increase mPTP activation, which permits mtDNA release into the cytoplasm [38]. Therefore, we sought to determine whether Ca^{2+} dynamics were disturbed in this study by stimulating inflammation. TEM indicated that LPS induced swelling and elongation of mitochondria, and increased ER-mitochondrial membrane apposition (Fig. 5c). In addition, we also observed matrix granules in H-PDLSCs + LPS cells, which is an important indicator of cationic poisoning (Fig. 5c, green arrows) [39]. Based on these observations, we measured the mitochondrial matrix Ca^{2+} concentration in H-PDLSCs and H-PDLSCs + LPS by Rhod-2 AM staining, and found that cells from the H-PDLSCs + LPS group exhibited significantly higher Ca^{2+} levels than those from the H-PDLSCs group (Fig. 5d). To investigate whether Ca^{2+} overloading induced mPTP opening, we performed Calcein-$CoCl_2$ staining. The confocal images and flow cytometric analysis revealed decreased calcein fluorescence intensity in the H-PDLSCs + LPS group, indicating increased mPTP opening (Fig. 5e). Importantly, RU360, which blocks Ca^{2+} uptake into mitochondria, effectively inhibited mPTP opening (Fig. S9), which demonstrated that Ca^{2+} overload induced mPTP opening in PDLSCs under LPS stimulation. In agreement with this, pharmacological blocking of mPTP opening with CsA prevented cGAS-STING axis activation to some extent in H-PDLSCs + LPS cells (Fig. 5f), and alleviated the osteogenic differentiation defect of PDLSCs under inflammation conditions significantly (Fig. 5g, Fig. S10). In addition, we examined the therapeutic effect of topical CsA application in mice with ligature-induced periodontitis. We found that CsA prevented the alveolar bone loss (Fig. 5h), as shown by the significantly lower CEJ-ABC distance, and the increase in BV/TV and Tb.Th in CsA treated mice (Fig. 5i). Moreover, given that CsA is an immunosuppressant, we also examined the long-term safety of CsA application at the animal level, results showed no obvious histopathological changes in the major organs after topical oral application of CsA (Fig. S11). Thus, we concluded that in inflammatory conditions, the increased colocalization of the ER and mitochondria results in mitochondrial Ca^{2+} overloading, which induces mPTP opening and cytosolic mtDNA leakage, and thus activates the cGAS-STING pathway.

3.5. cGAMP homeostasis disturbance results in the continuous activation of cGAS-STING pathway in PDLSCs

After cGAS binds to cytosolic mtDNA, it catalyzes the formation of the innate immune secondary messenger cGAMP, which is an immunotransmitter that activates innate immunity. Under physiological conditions, the immune system strikes a careful balance between launching a robust response to threats and avoiding over-activation as it could trigger devastating inflammation when not properly regulated. Therefore, we measured the intracellular and extracellular concentrations of cGAMP at different time points upon LPS stimulation using a sensitive cGAMP ELISA kit. We found that the extracellular concentration of cGAMP in the H-PDLSCs + LPS group was much lower than that of the H-PDLSCs group on day 3, 5, 7, whereas the intracellular cGAMP concentration for the H-PDLSCs + LPS group was significantly higher than that of the H-PDLSCs group on day 5, 7 (Fig. 6a). These findings indicated that the balance of cGAMP homeostasis in PDLSCs was severely disrupted. Possible mechanisms for the alterations in cGAMP levels are reduced transport and/or decreased extracellular degradation of cGAMP which would expose PDLSCs to high cytosolic cGAMP concentrations and cause cGAS-STING activation and cell dysfunction.

Although the molecular mechanisms of cGAMP export have not been fully revealed, plenty of evidence indicates that the ATP-binding cassette transporter ABCC1 could mediate cGAMP exportation [40]. Therefore, we measured the expression of ABCC1 and found that LPS exposure significantly decreased the ABCC1 expression (Fig. 6b). WB further verified the significant declined expression of ABCC1 (Fig. 6c and d). In addition, the expression of ENPP1, the extracellular hydrolase of cGAMP, in the H-PDLSCs + LPS group was also significantly reduced (Fig. 6e). Based on these findings, we hypothesized that the deficiency of ABCC1-mediated exportation and ENPP1-mediated degradation of cGAMP resulted in the accumulation of intracellular cGAMP, thereby triggering the sustained STING signaling activation in PDLSCs. Then, an ABCC1 agonist, TT [40], was applied to enhance cGAMP exportation. To do this, we initially checked the cytotoxicity of TT in PDLSCs using a CCK-8 assay, and found that concentrations of 1.0 μg/mL TT and below showed minimal toxicity towards PDLSCs (Fig. S12a). Additionally, 1 μg/mL TT significantly increased the extracellular cGAMP as shown in Fig. 6f. We then treated PDLSCs with 1 μg/mL TT and different concentration of ENPP1 protein, and found that the combination of 1 μg/mL TT and ENPP1 (0.2, 0.1, 0.05 μg/mL) significantly rescued the intracellular cGAMP stress (Fig. S12b), and we finally chose 1 μg/mL TT and 0.1 μg/mL ENPP1 for further experiments (Fig. 6g). We found that the combination of 1 μg/mL TT and 0.1 μg/mL ENPP1 not only effectively inhibited the activation of cGAS-STING pathway (Fig. 6h), but also rescued the osteogenic ability of PDLSCs (Fig. 6i, Fig. S12c). Overall, these findings suggested that the disturbance of cGAMP homeostasis resulted in the continuous activation of STING signaling and thus impeded the function of PDLSCs.

3.6. Restoring cGAMP homeostasis via CsA-TT-ENPP1@PEGA hydrogel inhibits cGAS-STING pathway and facilitates periodontal recovery in vivo

Based on our findings of cGAMP homeostasis related dysfunction of PDLSCs, we synthesized drug-loaded hydrogel system to precisely reestablish cGAMP homeostasis via manipulating its production, exocytosis and degradation for effective therapy of periodontitis. In brief, we prepared the PEGA based delivery system by mixing PEGA powder and photo initiator lithium phenyl-2,4,6-trimethylbenzoylphosphinate (LAP) and then ultrasonic cracking 5 min to form a photocurable aqueous solution. Subsequently, the mixture loaded with drug was cured under blue-light irradiation for 5 s (Fig. 7a). To evaluate the effect of the LAP concentration on the mechanical properties of the PEGA hydrogel, we mixed PEGA with LAP at different concentrations (0.07 %, 0.7 %, 7 %). We found that the LAP concentration had no significant influence on the storage modulus (G′) or loss modulus (G′′) of the PEGA hydrogel (Fig. 7b and c. Fig. S13a). In addition, we also characterized the micro-structure of the PEGA hydrogel with different LAP concentrations (0.07 %, 0.7 %, 7 %) by scanning electron microscopy (SEM), and observed that the LAP concentration did not affect the pore size or the porosity ratio (Fig. 7d, Fig. S13b). Therefore, we chose 0.07 % LAP to form the PEGA hydrogel. Energy dispersive spectrometry (EDS) analysis demonstrated the presence of four elements (C, N, O and Cl) in PEGA (Fig. 7e). To assess whether the PEGA hydrogels could maintain injectability and gelation properties to accommodate the defects with irregular shapes in periodontal tissues, both *in vivo* and *in vitro* tests were carried out. The hydrogels were injected into a 3D mold and rat skin tissues with different defect shapes. We found that after injection, the hydrogel solution filled the 3D models precisely (Fig. 7f). Additionally, the hydrogel quickly filled the defects and solidified following blue light radiation *in vivo* (Fig. S14). These results evidenced that the drug delivery hydrogel could easily adapt to irregularly shaped periodontal defects, enabling accurate filling and drug delivery. Fourier transform infrared spectroscopy (FTIR) of PEG powder showed that the absorption peaks at 2861 cm^{-1} overlapped each other, which was attributed to the C-H stretching vibration, and the absorption peaks at 1466 cm^{-1}, 1343 cm^{-1}, and 962/841 cm^{-1} were related to the bending vibration mode, out-of-plane, and in-plane rocking vibration modes of the PEG methylene group, respectively. The absorption peak at 1100 cm^{-1} was due to the stretching vibration of the C-O bond in PEG. In addition, there were two obvious absorption peaks at 1732 cm^{-1} and 1651 cm^{-1}, which are typical of the stretching vibration of the acid ester compound carbonyl C=O group.

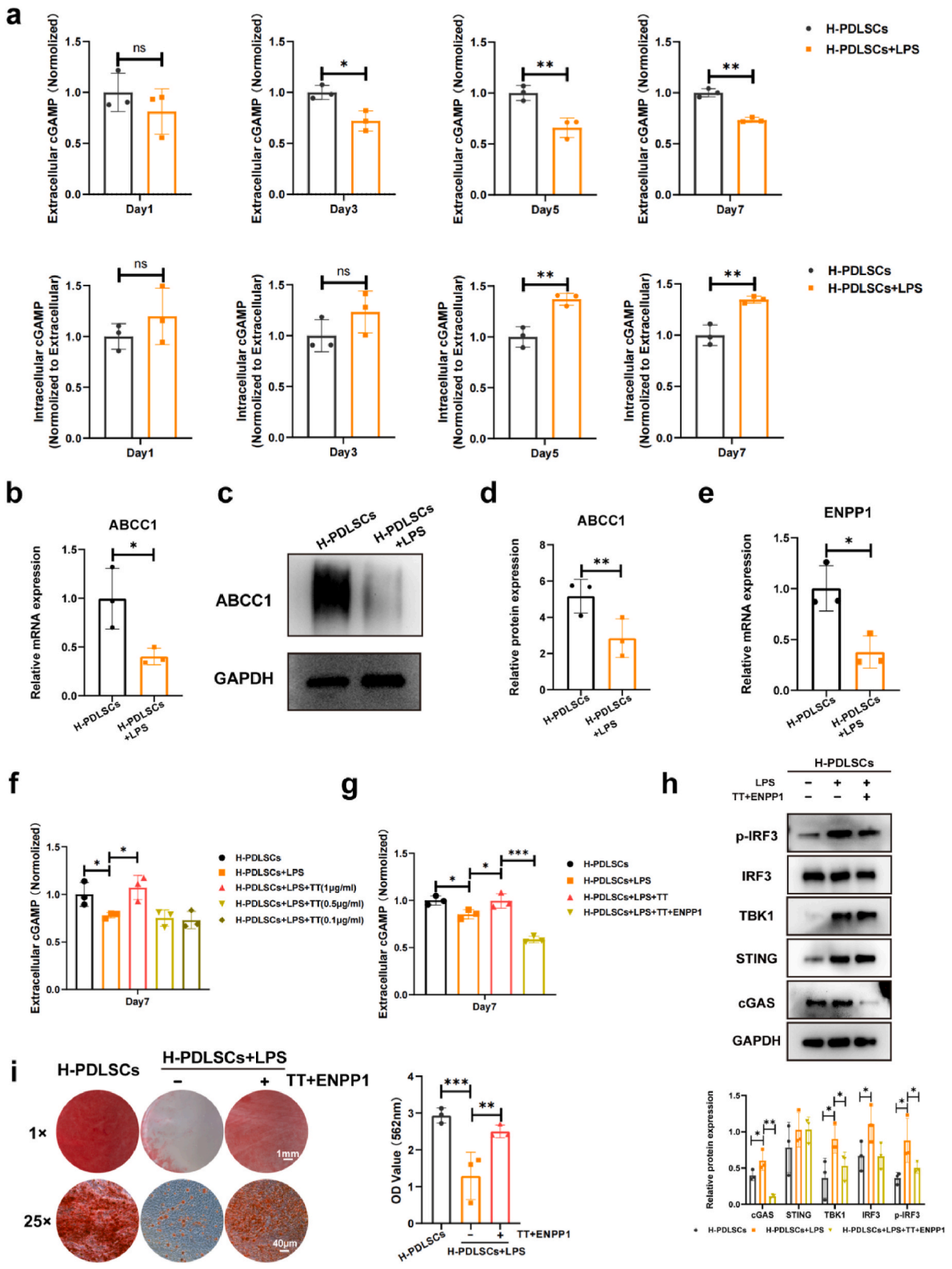

Fig. 6. Disturbance of cGAMP homeostasis results in intracellular cGAS-STING pathway activation. (a) ELISA analysis of the extracellular and intracellular cGAMP levels in the H-PDLSC and H-PDLSC + LPS groups over time. **(b)** Expression of ABCC1 mRNA quantified by qRT-PCR. **(c, d)** WB analysis of ABCC1 expression. **(e)** Expression of ENPP1 mRNA quantified by qRT-PCR. **(f)** ABCC1 agonist TT promotes extracellular transport of cGAMP. **(g)** Extracellular cGAMP detection after combination application of TT and ENPP1. **(h)** WB analysis of the cGAS-STING pathway after combination application of TT and ENPP1. **(i)** AR staining and quantitative analysis of mineralized nodules. $^{*}P < 0.05$, $^{**}P < 0.01$, $^{***}P < 0.001$, ns, not significant.

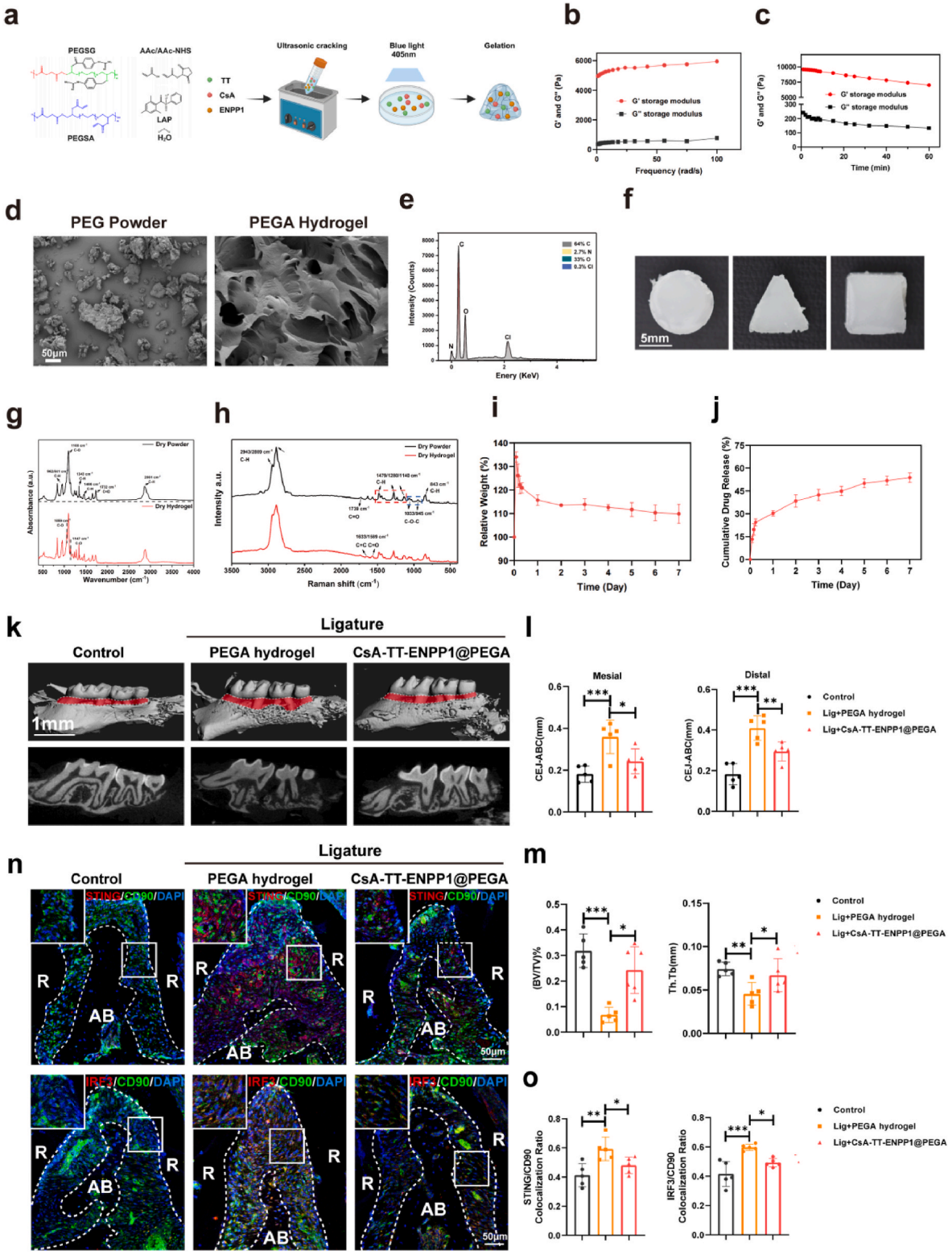

Fig. 7. CsA-TT-ENPP1@PEGA hydrogel restores cGAMP homeostasis and facilitates periodontal regeneration. **(a)** Schematic diagram of PEGA hydrogel synthesis. **(b)** Variation of the storage modulus and loss modulus (G′ and G′′) of the PEGA hydrogel under 5 % strain. **(c)** Variation of the storage modulus and loss modulus (G'and G'') in a time sweep of the PEGA hydrogel under 5 % strain and 6 rad/s **(d)** SEM images of PEG powder and PEGA hydrogel. Scale bar, 50 μm. **(e)** EDS spectrum of PEGA. **(f)** Photographs of injectable PEGA hydrogel on different 3D patterns *in vitro*. Scale bar, 5 mm. **(g)** FTIR spectra and **(h)** Raman spectra of PEG powder and the PEGA hydrogel. **(i)** Swelling and degradation curves of the PEGA hydrogel in PBS. **(i)** Cumulative release profile of DOX from the PEGA hydrogel. **(k)** Representative Micro-CT images of the alveolar bone of mice from different treatment groups. Scale bar, 1 mm. **(l)** Quantitative analysis of the CEJ-ABC. **(m)** Quantitative analysis of the BV/TV % and Th.Tb. **(n)** IF staining of PDLSCs (CD90, green) and STING (STING, red) in the periodontal tissue of mice from the different treatment groups. R: root, AB: alveolar bone. **(o)** Colocalization analysis of CD90 positive cells and STING positive cells. $^{*}P < 0.05$, $^{**}P < 0.01$, $^{***}P < 0.001$, ns, not significant.

Compared with the PEG powder, however, the C-O absorption peak at 1059 cm^{-1} and 1147 cm^{-1} of the PEGA hydrogel powder was shifted sharply, which may be due to the destruction of hydrogen bonds and other weak interactions between PEG molecules during the solidification process, but the infrared spectrum of the PEGA hydrogel still showed the typical characteristics of PEG (Fig. 7g). Raman spectra analysis also showed typical characteristics of PEG, but the relative intensity of the C=C or C=O signals at 1633/1569 cm^{-1} was weakened and the peak position was changed in the PEGA hydrogel, indicating that C=C or C=O bonds had participated in the reaction during the solidification process (Fig. 7h). To test the swelling of the PEGA hydrogel, we soaked the hydrogel in phosphate buffered saline (PBS) and observed that the hydrogel swells to the maximum weight and volume within 2 h and degrades slowly over a period of a week (Fig. 7i, Fig. S15). Based on the degradability of the PEGA hydrogel, we then tested the drug release properties and observed that about 36 % of the drug doxycycline was released in the first day and about 60 % in a week, which showed that after a rapid initial release, the PEGA hydrogel could release drug slowly and uniformly (Fig. 7j). These results indicated that the PEGA hydrogel is an ideal scaffold for localized drug release in irregular periodontal defects, as it can achieve good filling of periodontal defects, it degrades appropriately, and after initial rapid dosing has a slow and uniform drug release pattern.

Based on our findings, we then tested the *in vivo* therapeutic effect of combination of CsA, TT and ENPP1 in mice with ligature-induced periodontitis. We first examined the long-term safety of CsA-TT-ENPP1@PEGA *in vivo*. H&E staining showed no significant differences in the major organs after CsA-TT-ENPP1@PEGA injection for one month, suggesting the good biosafety of CsA-TT-ENPP1@PEGA (Fig. S16). Afterwards, CsA, TT and ENPP1 were added to the PEGA to fabricate the CsA-TT-ENPP1@PEGA hydrogel, and then injected into the periodontal tissue of periodontitis mice. Micro-CT examination indicated that there was much more osteogenesis in the CsA-TT-ENPP1@PEGA hydrogel group of mice than in the PEGA hydrogel alone group (Fig. 7k). In addition, the CEJ-ABC distance in the CsA-TT-ENPP1@PEGA hydrogel group was shorter than that in the PEGA hydrogel group (Fig. 7l). The BV/TV % and Tb.Th in CsA-TT-ENPP1@PEGA hydrogel group were also improved compared to the PEGA hydrogel group (Fig. 7m). In addition, IF showed that in the CsA-TT-ENPP1@PEGA hydrogel group, the expression of STING and IRF3 in CD90 marked PDLSCs was significantly extenuated (Fig. 7n and o). All the results confirmed that local cGAS-ABCC1-ENPP1 delivery could relieve periodontal tissue inflammation and promote alveolar bone regeneration. To summarize, we found that the cGAMP homeostasis plays a vital role in periodontitis, and restoring cGAMP homeostasis has great potential for the treatment of periodontitis.

4. Discussion

The cGAS-STING pathway is involved in a variety of inflammation-related diseases, such as AMD [41], systemic lupus erythematosus [42], Parkinson's disease [43] and acute kidney injury [44]. Most studies highlight the pro-inflammatory effect of the cGAS-STING pathway in immune cells [45]. MSCs are crucial for immune modulation and tissue regeneration in the inflammatory micro-environment [46,47]. However, the effect of the cGAS-STING pathway on the function of MSCs has not been completely elucidated. In the present study, we found that the cGAS-STING pathway was activated in inflamed PDLSCs, which are tissue specific MSCs, and genetic or pharmacological suppression of STING could prevent the osteogenic differentiation defect of inflamed PDLSCs. STING-disrupted mice were protected from ligature-induced periodontitis unlike control mice. Topical application of C176 could also facilitate periodontal tissue regeneration in mice. Together, these results indicate that STING plays an important role in PDLSC function and suggest that the cGAS-STING pathway is a potential therapeutic target for enhancing the osteogenic capability of PDLSCs.

Mitochondrial homeostasis is an essential prerequisite for normal stem cell differentiation [48–50]. Recently, several studies have demonstrated that mitochondrial damage plays a crucial role in the compromised function of PDLSCs [51,52], however, the underlying mechanisms are not completely understood. Consistent with our previous study, we found that LPS induced mitochondrial membrane potential depolarization, ROS accumulation, and mitochondrial Ca^{2+} overload [12]. We also found mtDNA leakage into the cytoplasm followed by mitochondria damage, which suggested that the activation of the cGAS-STING pathway is associated with cytosolic mtDNA accumulation. In addition, mtDNA depletion by EtBr alleviated the PDLSC osteogenic differentiation defect. These results supported our hypothesis that mtDNA cytosol translocation caused the activation of the cGAS-STING pathway in PDLSCs which impeded alveolar bone regeneration in periodontitis. Thus, PDLSC function is linked to mitochondria related innate immune dysregulation.

Current evidence indicates that different channels allow the efflux of mtDNA under different stress conditions and thus mediate the downstream signaling events. For instance, it has been reported that recruitment of BAX and BAK to the outer mitochondrial membrane (OMM) releases mtDNA by forming macropores in the OMM [53,54]. Also, under some stress conditions, such as mitochondrial Ca^{2+} overload [55], mitochondrial inner membrane instability may induce the mPTP channel to open followed by mtDNA release into the cytoplasm. Oligomerization of the VDAC channel could also mediate mtDNA release during oxidative stress [56]. Our previous study demonstrated that PDLSC dysfunction in inflammatory environments was accompanied by mitochondrial Ca^{2+} overload [12], which can activate the mPTP opening [57,58]. Here, in this study, we demonstrated that LPS induced mPTP opening, which increased mitochondrial permeability and permitted mtDNA release in PDLSCs. Furthermore, the inhibition of mPTP opening with CsA downregulated the cGAS-STING pathway and rescued the PDLSC osteogenic differentiation. These results indicated that LPS induced mtDNA leakage through mPTP. It is important to note here that CsA is an immunosuppressant. In this study, the 10 mg/kg dose of CsA used *in vivo* was chosen based on previous studies [26,27,59], and the CsA treatment was administered locally via periodontal injection for a short duration (10 mg/kg/day for only 7 days). No side effects, such as flora imbalances or fungal infections, were observed at this dose, as reported in prior studies and our own research. Moreover, both CsA injection alone and CsA loaded in CsA-TT-ENPP1@PEGA demonstrated good biosafety. However, we will continue to monitor these factors in future studies.

cGAMP is a key component in cGAS-STING pathway activation and is synthesized by cGAS upon stimulated by cytosolic DNA [60]. After confirming mtDNA release under inflammatory stimuli, we measured the cGAMP levels both inside and outside the cell. We found elevated levels of intracellular cGAMP, but the extracellular cGAMP concentration decreased over time. The extracellular cGAMP can be hydrolyzed by ENPP1 [61]. However, we found that ENPP1 was decreased in inflamed PDLSCs, indicating that the reduction in cGAMP may be due to its transportation. Intriguingly, the cGAMP transport channel ABCC1 was significantly downregulated under inflammatory conditions, suggesting that the transportation of cGAMP was inhibited when the production of cGAMP was increased by mtDNA release.

Currently, many therapeutic approaches target the STING pathway, e.g., by activating the STING pathway in immune cells or in tumor cells to activate the immune killing of tumors [62]. However, few therapeutic strategies are aimed inhibiting the STING pathway. Recently, a nanomaterial, Platinum-doped positively charged carbon dots (Pt-CDs), has been designed to treat psoriasis by inhibiting the cGAS-STING pathway via removing upregulated cell-free DNA (cfDNA) as well as ROS in the inflammatory environment [63]. Existing studies have only focused on activating the upstream components of the cGAS-STING pathway, while the question of how cGAMP, which has is generated by cfDNA stimulation, can be scavenged remains to be addressed. Indeed, the

accumulation of cGAMP is precisely the key to the sustained activation of the cGAS-STING pathway. In this study, based on our discovery of the mechanism of cGAMP homeostatic imbalance in inflammatory PDLSCs, we constructed a drug-loaded hydrogel that can be locally injected in the periodontium and promote periodontal recovery. Although the injection of C176 can attenuate periodontal damage by inhibiting STING activation, it does not fully block the upstream mechanisms that trigger STING activation. Consequently, continuous injection of C176 is required to sustain its therapeutic effects. In contrast, the CsA-TT-ENPP1@PEGA hydrogel provides a more comprehensive approach by regulating cGAMP production, transport, and degradation, thus more effectively modulating STING activation. By restoring cGAMP homeostasis, the hydrogel enhances stem cell function and prevents chronic STING activation, addressing the underlying cause of inflammation. Moreover, the hydrogel forms at the target site and enables sustained, controlled release of CsA, TT, and ENPP1, offering long-term therapeutic effects with a single administration. This not only reduces the frequency of dosing but also ensures more stable local drug concentrations, enhancing treatment efficacy over time. Therefore, while both the CsA-TT-ENPP1@PEGA hydrogel and C176 show similar therapeutic outcomes, the hydrogel's ability to more comprehensively block upstream STING activation, combined with its convenient, long-term delivery profile, positions it as a more promising solution for periodontal tissue regeneration and long-term disease management.

5. Conclusion

In this work, we have established a link between the cGAMP homeostasis and the function of MSCs. Furthermore, it is first found in this study that inflammation can induce mtDNA cytosolic release, downregulate the expression of ABCC1 and decrease the level of ENPP1, which are responsible for the accumulation of cGAMP, thereby leading to the persistent activation of the cGAS-STING pathway and impaired the differentiation capacity of PDLSCs. This study not only introduces novel methodologies for periodontal regeneration but also proposes innovative strategies for the management of other inflammation-related diseases.

CRediT authorship contribution statement

Xiang Liu: Writing – original draft, Investigation, Data curation, Formal analysis, Software, Validation, Writing – review & editing. **Hua Zhang:** Resources, Supervision, Validation, Writing – original draft, Writing – review & editing. **Lei Xu:** Software, Visualization, Writing – original draft, Writing – review & editing. **Huayu Ye:** Supervision, Visualization. **Jinghuan Huang:** Methodology. **Jing Xiang:** Supervision, Visualization. **Yunying He:** Investigation. **Huan Zhou:** Supervision, Visualization. **Lingli Fang:** Resources. **Yunyan Zhang:** Supervision, Visualization. **Xuerong Xiang:** Supervision, Conceptualization. **Richard D. Cannon:** Supervision, Conceptualization. **Ping Ji:** Writing – review & editing, Supervision, Funding acquisition, Visualization. **Qiming Zhai:** Writing – review & editing, Supervision, Funding acquisition, Conceptualization, Methodology, Validation.

Data availability statement

The data that support the findings of this study are available from the corresponding author upon reasonable request. All other data are provided in the main text or the supplemental materials.

Ethics approval and consent to participate

The experiment procedures were approved by the Stomatological Hospital of Chongqing Medical University (CQHS-REC-2024–038).

Declaration of competing interest

The authors declare that they have no known competing financial interests or personal relationships that could have appeared to influence the work reported in this paper.

Acknowledgement

This study was sponsored by the National Natural Science Foundation of China (82220108019 to P. Ji and 82201059 to Q.M. Zhai), the Chongqing Postdoctoral Science Special Foundation (2021XM1031 to Q. M. Zhai), and China Postdoctoral Science Foundation (2022M720599 to Q.M. Zhai). Haobo medical technology (Shanghai) limited company helped us synthesize the PEGA materials.

Appendix A. Supplementary data

Supplementary data to this article can be found online at https://doi.org/10.1016/j.bioactmat.2025.02.010.

References

[1] L. Xin, et al., Four-Octyl itaconate ameliorates periodontal destruction via Nrf2-dependent antioxidant system, Int. J. Oral Sci. 14 (1) (2022) 27.
[2] B.T. Rosier, P.D. Marsh, A. Mira, Resilience of the oral microbiota in Health: mechanisms that prevent dysbiosis, J. Dent. Res. 97 (4) (2018) 371–380.
[3] M. Di Stefano, et al., Impact of oral microbiome in periodontal Health and periodontitis: a critical review on prevention and treatment, Int. J. Mol. Sci. 23 (9) (2022).
[4] F. Lei, et al., Treatment of inflammatory bone loss in periodontitis by stem cell-derived exosomes, Acta Biomater. 141 (2022) 333–343.
[5] Q. Zhai, et al., Dental stem cell and dental tissue regeneration, Front. Med. 13 (2) (2019) 152–159.
[6] X. Li, et al., LncRNA GACAT2 binds with protein PKM1/2 to regulate cell mitochondrial function and cementogenesis in an inflammatory environment, Bone Res. 10 (1) (2022) 29.
[7] Y. Liu, et al., Clathrin-associated AP-1 controls termination of STING signalling, Nature 610 (7933) (2022) 761–767.
[8] L.S. Huang, et al., mtDNA activates cGAS signaling and suppresses the YAP-mediated endothelial cell proliferation program to promote inflammatory injury, Immunity 52 (3) (2020) 475–486e5.
[9] D. Zhang, et al., A non-canonical cGAS-STING-PERK pathway facilitates the translational program critical for senescence and organ fibrosis, Nat. Cell Biol. 24 (5) (2022) 766–782.
[10] J. Willemsen, et al., TNF leads to mtDNA release and cGAS/STING-dependent interferon responses that support inflammatory arthritis, Cell Rep. 37 (6) (2021) 109977.
[11] Z. Liu, et al., XBP1 deficiency promotes hepatocyte pyroptosis by impairing mitophagy to activate mtDNA-cGAS-STING signaling in macrophages during acute liver injury, Redox Biol. 52 (2022) 102305.
[12] Q. Zhai, et al., Nanorepairers rescue inflammation-induced mitochondrial dysfunction in mesenchymal stem cells, Adv. Sci. 9 (4) (2022) e2103839.
[13] C. Chen, P. Xu, Cellular functions of cGAS-STING signaling, Trends Cell Biol. 33 (8) (2023) 630–648.
[14] C. Zhou, et al., Transfer of cGAMP into bystander cells via LRRC8 volume-regulated anion channels augments STING-mediated interferon responses and anti-viral immunity, Immunity 52 (5) (2020) 767–781e6.
[15] L.J. Lahey, et al., LRRC8A:C/E heteromeric channels are ubiquitous transporters of cGAMP, Mol. Cell 80 (4) (2020) 578–591e5.
[16] J.H. Maltbaek, et al., ABCC1 transporter exports the immunostimulatory cyclic dinucleotide cGAMP, Immunity 55 (10) (2022) 1799–1812e4.
[17] J. Li, et al., Metastasis and immune evasion from extracellular cGAMP hydrolysis, Cancer Discov. 11 (5) (2021) 1212–1227.
[18] L. Lin, et al., UCHL1 impairs periodontal ligament stem cell osteogenesis in periodontitis, J. Dent. Res. 102 (1) (2023) 61–71.
[19] Y.Y. Zhang, et al., Fumarate restrains alveolar bone restoration via regulating H3K9 methylation, J. Dent. Res. 103 (12) (2024) 1302–1312.
[20] Y. Hu, et al., Human gingival mesenchymal stem cell-derived exosomes cross-regulate the Wnt/β-catenin and NF-κB signalling pathways in the periodontal inflammation microenvironment, J. Clin. Periodontol. 50 (6) (2023) 796–806.
[21] X. Liu, et al., Piezoelectric hydrogel for treatment of periodontitis through bioenergetic activation, Bioact. Mater. 35 (2024) 346–361.
[22] M. Moriyama, T. Koshiba, T. Ichinohe, Influenza A virus M2 protein triggers mitochondrial DNA-mediated antiviral immune responses, Nat. Commun. 10 (1) (2019) 4624.
[23] C.H. Yu, et al., TDP-43 triggers mitochondrial DNA release via mPTP to activate cGAS/STING in ALS, Cell 183 (3) (2020) 636–649e18.
[24] X. Liu, et al., Bioinspired Andrias davidianus-Derived wound dressings for localized drug-elution, Bioact. Mater. 15 (2022) 482–494.

[25] Y.T. Shi, et al., Ligature-induced periodontitis drives colorectal cancer: an experimental model in mice, J. Dent. Res. 102 (6) (2023) 689–698.
[26] J. Zalewski, et al., Cyclosporine A reduces microvascular obstruction and preserves left ventricular function deterioration following myocardial ischemia and reperfusion, Basic Res. Cardiol. 110 (2) (2015) 18.
[27] V. Rusinkevich, et al., Temporal dynamics of immune response following prolonged myocardial ischemia/reperfusion with and without cyclosporine A, Acta Pharmacol. Sin. 40 (9) (2019) 1168–1183.
[28] Y. Peng, et al., Stimulator of IFN genes mediates neuroinflammatory injury by suppressing AMPK signal in experimental subarachnoid hemorrhage, J. Neuroinflammation 17 (1) (2020) 165.
[29] B. Han, et al., Pulmonary inflammatory and fibrogenic response induced by graphitized multi-walled carbon nanotube involved in cGAS-STING signaling pathway, J. Hazard Mater. 417 (2021) 125984.
[30] H. Huang, et al., Nanoparticulate cell-free DNA scavenger for treating inflammatory bone loss in periodontitis, Nat. Commun. 13 (1) (2022) 5925.
[31] Y. Mao, et al., STING-IRF3 triggers endothelial inflammation in response to free fatty acid-induced mitochondrial damage in diet-induced obesity, Arterioscler. Thromb. Vasc. Biol. 37 (5) (2017) 920–929.
[32] R.P. Chakrabarty, N.S. Chandel, Mitochondria as signaling organelles control mammalian stem cell fate, Cell Stem Cell 28 (3) (2021) 394–408.
[33] M.C. Ludikhuize, et al., Mitochondria define intestinal stem cell differentiation downstream of a FOXO/notch Axis, Cell Metab. 32 (5) (2020) 889–900e7.
[34] K. Wei, et al., Mitochondrial DNA release via the mitochondrial permeability transition pore activates the cGAS-STING pathway, exacerbating inflammation in acute Kawasaki disease, Cell Commun. Signal. 22 (1) (2024) 328.
[35] T. Yamazaki, et al., Mitochondrial DNA drives abscopal responses to radiation that are inhibited by autophagy, Nat. Immunol. 21 (10) (2020) 1160–1171.
[36] S. Victorelli, et al., Apoptotic stress causes mtDNA release during senescence and drives the SASP, Nature 622 (7983) (2023) 627–636.
[37] D. Zhang, et al., Mitochondrial Ca(2+) homeostasis: emerging roles and clinical significance in cardiac remodeling, Int. J. Mol. Sci. 23 (6) (2022).
[38] T.M. Bauer, E. Murphy, Role of mitochondrial calcium and the permeability transition pore in regulating cell death, Circ. Res. 126 (2) (2020) 280–293.
[39] O. Gerasimenko, A. Tepikin, How to measure Ca2+ in cellular organelles? Cell Calcium 38 (3–4) (2005) 201–211.
[40] M. Wā̦lfl-Duchek, et al., Use of PET imaging to assess the efficacy of thiethylperazine to stimulate cerebral MRP1 transport activity in wild-type and APP/PS1-21 mice, Int. J. Mol. Sci. 23 (12) (2022).
[41] W. Ouyang, et al., The cGAS-STING pathway-dependent sensing of mitochondrial DNA mediates ocular surface inflammation, Signal Transduct. Targeted Ther. 8 (1) (2023) 371.
[42] M. Motwani, et al., cGAS-STING pathway does not promote autoimmunity in murine models of SLE, Front. Immunol. 12 (2021) 605930.
[43] B. Wang, et al., The STING inhibitor C-176 attenuates MPTP-induced neuroinflammation and neurodegeneration in mouse parkinsonian models, Int. Immunopharmacol. 124 (Pt A) (2023) 110827.
[44] J. Li, et al., Phosphoglycerate mutase 5 initiates inflammation in acute kidney injury by triggering mitochondrial DNA release by dephosphorylating the pro-apoptotic protein Bax, Kidney Int. 103 (1) (2023) 115–133.
[45] M.F. Gulen, et al., cGAS-STING drives ageing-related inflammation and neurodegeneration, Nature 620 (7973) (2023) 374–380.
[46] P. Chen, et al., Single-cell and spatial transcriptomics decodes wharton's jelly-derived mesenchymal stem cells heterogeneity and a subpopulation with wound repair signatures, Adv. Sci. 10 (4) (2023) e2204786.
[47] W. Jiang, J. Xu, Immune modulation by mesenchymal stem cells, Cell Prolif. 53 (1) (2020) e12712.
[48] W. Cai, et al., Mitochondrial transfer regulates cell fate through metabolic remodeling in osteoporosis, Adv. Sci. 10 (4) (2023) e2204871.
[49] S. Yao, et al., Nestin-dependent mitochondria-ER contacts define stem Leydig cell differentiation to attenuate male reproductive ageing, Nat. Commun. 13 (1) (2022) 4020.
[50] M. Xu, et al., L-arginine homeostasis governs adult neural stem cell activation by modulating energy metabolism in vivo, EMBO J. 42 (6) (2023) e112647.
[51] H. Fang, et al., Glycosylation end products mediate damage and apoptosis of periodontal ligament stem cells induced by the JNK-mitochondrial pathway, Aging (Albany NY) 12 (13) (2020) 12850–12868.
[52] T. Lan, et al., PPAR-İţ activation promotes xenogenic bioroot regeneration by attenuating the xenograft induced-oxidative stress, Int. J. Oral Sci. 15 (1) (2023) 10.
[53] K. Cosentino, et al., The interplay between BAX and BAK tunes apoptotic pore growth to control mitochondrial-DNA-mediated inflammation, Mol. Cell 82 (5) (2022) 933–949.e9.
[54] S. Li, et al., SFTSV infection induces BAK/BAX-Dependent mitochondrial DNA release to trigger NLRP3 inflammasome activation, Cell Rep. 30 (13) (2020) 4370–4385e7.
[55] R.J. Parks, et al., Cyclophilin D-mediated regulation of the permeability transition pore is altered in mice lacking the mitochondrial calcium uniporter, Cardiovasc. Res. 115 (2) (2019) 385–394.
[56] H. Zhou, et al., Melatonin protects cardiac microvasculature against ischemia/reperfusion injury via suppression of mitochondrial fission-VDAC1-HK2-mPTP-mitophagy axis, J. Pineal Res. 63 (1) (2017).
[57] Y. Zhou, et al., Double-activation of mitochondrial permeability transition pore opening via calcium overload and reactive oxygen species for cancer therapy, J. Nanobiotechnol. 20 (1) (2022) 188.
[58] R. Gordan, et al., Iron overload, oxidative stress and calcium mishandling in cardiomyocytes: role of the mitochondrial permeability transition pore, Antioxidants 9 (8) (2020).
[59] K. Niimi, et al., Mitochondrial permeability transition pore opening induces the initial process of renal calcium crystallization, Free Radic. Biol. Med. 52 (7) (2012) 1207–1217.
[60] Y. An, et al., Tumor exosomal ENPP1 hydrolyzes cGAMP to inhibit cGAS-STING signaling, Adv. Sci. 11 (20) (2024) e2308131.
[61] J.A. Carozza, et al., Extracellular cGAMP is a cancer cell-produced immunotransmitter involved in radiation-induced anti-cancer immunity, Nat. Can. (Ott.) 1 (2) (2020) 184–196.
[62] H. Jiang, et al., Nanocatalytic innate immunity activation by mitochondrial DNA oxidative damage for tumor-specific therapy, Adv. Mater. 33 (20) (2021) e2008065.
[63] Z. Zhang, et al., A nanoinhibitor targeting cGAS-STING pathway to reverse the homeostatic imbalance of inflammation in psoriasis, Angew Chem. Int. Ed. Engl. 63 (2) (2024) e202316007.